HELLENIC MEDITERRANEAN UNIVERSITY

DEPARTMENT OF ELECTRONIC ENGINEERING

MASTER THESIS

Experimental and numerical study of laser induced particle acceleration from solid targets.

Tazes Ioannis

Rethymno, 2019

HELLENIC MEDITERRANEAN UNIVERSITY

DEPARTMENT OF ELECTRONIC ENGINEERING

MASTER THESIS

Experimental and numerical study of laser induced particle acceleration from solid targets.

Tazes Ioannis

Advisory Committee

Prof. Michael Tatarakis

Prof. Vasilis Dimitriou

Prof. Emmanouil Benis

Acknowledgements

I would like to express my gratitude to my supervisor Prof. Michael Tatarakis for his support and essential guidance during my master thesis as well for the opportunities he provided me during my studies, and he continues to provide. I would like to thank Prof. Vasilis Dimitriou who introduced and guided me to numerical simulations as well as for his advices and constant feedback during every step of my master. In addition, thanks to Prof. Emmanouil Benis for his advices and fruitful comments on this thesis. I would also like to thank Dr. Eugene Clark for being there in every step of this master thesis as well as for our valuable discussions. Furthermore, I would like to thank Prof. Nektarios Papadogiannis for his advices and guidance.

I would like to extend a special thanks to Anastasios Grigoriadis and Georgia Andiranaki for our great teamwork and support. Moreover, I really appreciate the help of Stelios Petrakis, Ioannis Fitilis, Alekos Skoulakis, Evaggelos Kaselouris and everyone else of the team of IPPL.

Finally, a grateful thanks to my family for their love and support.

Abstract

The present thesis is focused on the investigation of the experiments performed in Institute of Plasma Physics & Lasers – IPPL by the interaction of "Zeus" a 45*TW* ultrafast laser with thin solid targets. Proton and electron particles were accelerated using Aluminum thin foil targets of a few μm thickness. The solid targets were irradiated by pulses of a few *fs* duration, with intensities above the $10^{20} W/cm^2$. Target Normal Sheath Acceleration - TNSA experiments were performed and proton beams of ~2*MeV*, as well as electron beams of hundreds keV (~600*keV)*, energies were correspondingly measured. The effects of an intense laser prepulse, preceding the peak intensity of the main laser pulse, on the acceleration of the particles, were also studied. This research was further extended to include Particle-In-Cell - PIC simulations in two dimensions, using the opensource advance relativistic EM MPI parallelized code EPOCH, developed under the Extendable PIC Open Collaboration project in UK. The effects of preplasma expansion for three characteristic target thicknesses and two representative pulse durations, were investigated. The simulation results highlight that under such extreme laser intensities, particle acceleration mechanisms beyond charge separation emerge.

Περίληψη

Σκοπός της παρούσας μεταπτυχιακής εργασίας είναι η πειραματική μελέτη της αλληλεπίδρασης των υπερβαχέων παλμών του “Zeus” 45TW laser του Ινστιτούτο Φυσικής Πλάσματος & Lasers – IPPL με λεπτούς στερεούς στόχους. Πρωτόνια και ηλεκτρόνια επιταχυνθήκαν από στόχους αλουμίνιου πάχους λίγων μm. Η στερεοί στόχοι ακτινοβολήθηκαν με παλμούς διαρκείας μερικών fs και ένταση άνω των $10^{20} W/cm^2$. Πειράματα με την τεχνική Target Normal Sheath Acceleration – TNSA πραγματοποιήθηκαν, οπού μετρήθηκαν δέσμες πρωτονίων ενέργεια ~2MeV καθώς και δέσμες ηλεκτρονίων ενέργειας εκατοντάδων keV (~600keV). Επίσης πραγματοποιήθηκε μελέτη της επίδρασης υψηλής έντασης προ-παλμού, ο οποίος καταφθάνει στον στόχο πριν τον κύριο παλμό, στην επιτάχυνση των σωματιδίων. Η έρευνα αύτη επεκτάθηκε περεταίρω με την υλοποίηση Particle-In-Cell – PIC δισδιάστατων προσομοιώσεων, με την χρήση του ανοιχτού σχετικιστικού EM MPI παράλληλου κώδικα EPOCH. Πραγματοποιήθηκε μελέτη των αποτελεσμάτων της εξάπλωσης προ-πλάσματος πριν την άφιξη του κύριου παλμού για τρεις στόχους διαφορετικού πάχους, καθώς και για δυο, διαφορετικής χρονικής διαρκείας, παλμούς. Τα αποτελέσματά των προσομοιώσεων υποδείξαν ότι επιπλέων μηχανισμοί επιτάχυνσης σωματιδίων, πέραν του TNSA, λαμβάνουν χώρα κατά τη χρήση τόσο ακραίων εντάσεων laser.

Table of Contents

List of figures

List of Symbols

a_0	Normalized vector potential	E	Electric field vector
c	Speed of light in a vacuum	E_0	Electric field magnitude
e	Electron charge	B	Magnetic field vector
F_p	ponderomotive force	c_s	Plasma speed of sound
I_p	ionization potential	v_{osc}	Oscillation velocity
I_L	laser intensity	$\hbar$	Reduced Plank's constant
k_b	Boltzmann constant	p	Momentum vector
m_e	Electron mass	u	Particle velocity
n	Index of refraction	P_c	Self focusing threshold power
n_e	Electron density	P	Laser power
n_i	Ion density	ω_L	Laser frequency
n_{cr}	Critical plasma density	ω_{pe}	Electron plasma frequency
Z	Ionization state	ω_{pi}	Ion Plasma frequency
γ	Keldish parameter	E_L	Laser energy
γ	Lorentz factor	U_p	Ponderomotive energy
ε_0	Vacuum permittivity	λ_D	Debye length
T_e	electron temperature		
T_{hot}	Hot electron temperature		

Chapter 1

1 Introduction

A new field of intense light interacting with matter was introduced, when T.H. Maiman [1] in 1960 invented laser. Ever since the laser technology is constantly improving and alongside, the achievable laser intensities. In 1985 the great leap on laser technology came with the conception of the Chirped Pulse Amplification - CPA technique by Mourou and Strickland [2]. This technique allowed the stretching of the pulse to intensities below the damage threshold of the laser optical components and after the amplification of the pulse energy, the recompression of the pulse, making possible laser intensities well above $10^{18} W/cm^2$. introducing the field of relativistic laser-plasma physics. CPA along with the development of Ti:Sapphire lasers in 1982 enabled the generation of pulses of few *fs* duration with high repetition rates and intensities above 10^{20} W/cm^2. Nowadays there are several *TW* and *PW* laser facilities worldwide delivering energies that range from a few *mJ* to hundreds of *J* and variable pulse durations.

Due to its numerus applications, charged particle acceleration has attracted great interest over the last decades. Laser-driven particle acceleration is considered to be a promising alternative to conventional particle accelerators. Conventional accelerators are large scale, high cost facilities, installed in hospitals for radiation therapy and/or used for fundamental physics research. Such an accelerator is the Large Hadron Collider LHC in CERN [3] with a diameter of ~27 kilometers. On the other hand, laser accelerators are compact tabletop devices, able to deliver high energy, quasi-monoenergetic, collimated electron or ion beams, as well as X-ray bursts.

With the current laser intensities electrons can be directly accelerated by the electric field of the lasers up to very high energies, above *GeV* [4]. The accelerated electrons are used in X-rays generated by synchrotron radiation. Laser plasma wakefield accelerators are able to deliver appreciably monoenergetic electrons beams of *GeV* energies over a small distance [4,5]. X-ray radiation is widely used in medical, X-ray imaging and many other applications.

Protons and ions are way heavier compared to electrons thus the current laser electric fields are not able to accelerate them. Various methods have been developed that accelerate ions with electric field generated from charge separation. Essentially, energetic electron bunches drag the plasma

ions and accelerate them indirectly. The Target Normal Sheath Acceleration - TNSA method is accelerating protons to energies of tens of *MeV's*. One of the most promising and challenging application of proton and ion acceleration is the hadron therapy [6,7]. Energetic ions have the unique ability to propagate deep, through matter and deposit their energy at the end of their travel, while the energy deposition is very low during propagation. This behavior of ions is known as the *Bragg peak*. The *Bragg peak*, provides to the ion beams the advantage of focusing and damaging tissue targets, allocated deep under the body skin, while the organic surroundings remain safe. This advantage turns the option of using ion acceleration favorable in comparison to the options of using X-rays or electron acceleration, that during their travel, deposit the major fraction of their energy on the targets surface and in trajectory. Although hadron therapy is performed by conversional accelerators, laser driven ion accelerator can significantly reduce the cost and the size of the accelerating facilities in the future. The main obstacle of laser driven hadron therapy [8] is that the achieved proton energies are not yet high enough. Until now, measured proton energies have exceeded 85*MeV* [9,10], although the energies demanded in medical applications are of the order of 250*MeV*. Additionally, in such applications the protons beams must be quasi-monoenergetic, tunable and able to be delivered in high repetition rates.

Proton radiography as a diagnostic technique in high energy density physics, is another application of ion acceleration, as well as laser plasma interaction and plasma induced electromagnetic field diagnostics [11,12]. The reason that makes protons appealing as an important diagnostic is that different energy protons probe the region of interest in different time frames. The most energetic protons capture the early moments of the studied phenomenon transient evolution, while the lower energy protons capture moments in later times, providing high temporal resolution.

The laser driven counterpart scheme of the magnetic confinement fusion that use huge high cost Tokamak or Stellarator reactors to confine plasma, is the Inertial Confinement Fusion - ICF. In ICF a small pellet of Deuterium and Tritium is isotropically compressed to very high densities. The compression is either applied by beams directly compressing the pellet, or indirectly by the laser beams irradiating the surrounding high Z material, known as holraum, and generate X-rays that in turn compress the fuel. If the degree of symmetry of the compression is not high enough, hydrodynamic instabilities rise, thus failing to achieve the densities required for fusion. If compression is adequate the ions will be sufficiently heated to overcome their Coulombic repulsion

and ignition will initialized. An alternative scheme of ICF is the promising Fast Ignition - FI scheme [13]. In FI, while the fuel compression is maximized, an energetic particle beam deposits a huge amount of energy into the fuel, assisting the ions acquire the necessary temperature to begin fusion. The energetic particle beam is either an electron beam (or alternative by proton beam) guided to the fuel core by a cone fitted to the pellet [14]. These proton beams are generated by intense laser beams irradiating a metallic solid target that is set close to the fuel. Proton beams do not need a guiding cone because of their *Bragg peak*, that enables them to deliver their energy directly, into the core of the fuel. ICF is studied at large facilities around the world such as National Ignition Facility NIF [14] in USA as well as the European proposed High Power laser Energy Research facility HiPER [15].

Many ion acceleration schemes have been proposed. In Coulomb explosion the target is stripped from its electrons due to the lasers pondermotive force. The electrostatic repulsion between the ions accelerates them to a form of explosion [16]. Another acceleration mechanism is the propagation of electrostatic shocks inside over- or under- dense plasma, also known as Collisionless electrostatic Shock Acceleration -CESA [17]. Radiation Pressure Acceleration - RPA [18,19] has also attracted great interest recently. RPA takes place when laser irradiance is extremely high, exerting great radiation pressure in the overdense plasma surface, accelerating ions in the forward direction due to charge separation. There are two regimes of RPA, the Hole-boring which occur on thick overdense targets and the light-sail [20] regime for very thin (~*nm*) targets. Usually more than one of those mechanisms coexist in any given ion acceleration experiment and it is not easy to distinguish the contribution of each one to the resulting overall acceleration. Various techniques to properly study them, like using circularly polarized light at normal incidence to suppress TNSA have been performed [18,21].

This Thesis is focused on the study of ultra-intense laser interaction with solid targets and the properties of the accelerated particle beams produced by that interaction. The TNSA mechanism is studied, as well as the effects of laser and target parameters, such as different pulse durations and target thicknesses, on the particle beams. The study was performed experimentally as well as numerically using Particle-In-Cell - PIC simulations. The experiments were performed in “Zeus”, a 45*TW* ultrafast, Ti:sapphire laser located at the Institute of Plasma Physics & Lasers – IPPL in Rethymnon, Crete.

Chapter 2

2 Laser Plasma Interaction

In this chapter, an introduction to plasma physics and laser-plasma interactions is provided. The fundamental concepts of plasma and its interactions with laser pulses are presented. The mechanisms of laser energy coupling into plasma electrons in different plasma densities are referred. The mechanisms of particle acceleration are also discussed.

2.1 Interactions of fs lasers with plasma

2.1.1 Ionization Processes

During the interaction of matter with strong electromagnetic fields, atomic ionization occurs, setting free the least bound electrons of the atom. The simplest case of ionization is the absorption of a single photon by the outermost electron of an atom, known as single photon ionization. Ionization can occur by absorbing a single high energy photon, or several low energy photons instead. This phenomenon is known as Multi-Photon Ionization - MPI and depends on the laser light intensity and/or photon density. At higher laser intensities, of the order of $10^{13} W/cm^2$, the laser field becomes comparable to the Coulomb potential of the atom, and new ionization mechanisms emerge. Agostini et al. in 1979 [22] experimentally observed electron energy spectra with distinct peaks above the ionization energy of the atoms, separated by one photon energy $\hbar\omega$. This phenomenon, is a branch of MPI with excess of photon, known as Above Threshold Ionization - MPI-ATI. ATI allows an electron to absorb more photons than those needed to get free from the parent atom and as a result the ionization potential I_p of the atom is increased. With even greater laser intensities, of the order $10^{14} W/cm^2$, Tunneling Ionization - TI [23] becomes the dominant ionization mechanism. During TI the Coulomb potential of the atom bends by the strong electric field of the laser. The suppressed potential of the atom acts as a finite potential barrier, as presented *figure 2-1*. Quantum mechanics dictates that the electron can tunnel through this barrier with a finite probability. The final ionization mechanism appears for intensities greater than $10^{16} W/cm^2$. The potential barrier of the atom, under laser electric fields of this magnitude is suppressed beyond the capability of holding the electron bound, as a result the electron escapes from the Coulomb well. This phenomenon is known as Over the Barrier Ionization-OTBI. For TI

or OTBI to occur, electrons must have enough time to move before the electric field of the laser reverses, thus the laser fundamental beam must have a slow oscillating frequency [23].

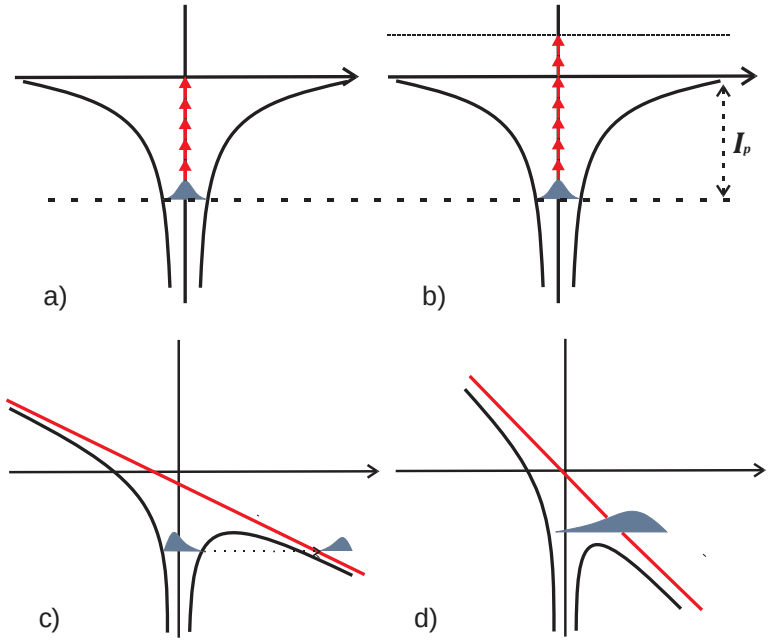

Figure 2-1: The ionization mechanisms a) multiphoton ionization - MPI, b) above threshold ionization - MPI-ATI c) tunnel ionization - TI and d) over the barrier ionization – OTBI [23].

Keldish [24] introduced the parameter γ to categorize which one of the ionization processes is the dominant, known as Keldish parameter and is given by:

$$\gamma = \sqrt{\frac{I_p}{2U_p}} \tag{2.1}$$

Where I_p is the ionization potential and U_p is the so-called ponderomotive energy of the electron, meaning the cycle-averaged quiver energy an electron gains in the presence of the laser's electric field:

$$U_p(eV) = \frac{e^2 E_0^2}{4 m_e \omega_L^2} \approx 9.33 \times 10^{-14} \times I_L \left[\frac{W}{cm^2}\right] \times \lambda_L^2 [\mu m^2] \tag{2.2}$$

where E_0 is the amplitude of the laser electric field, ω_L the frequency of the Electromagnetic field, I_L the lasers Intensity, λ is the wavelength of the laser, e and m_e the charge and mass of the electron. If $\gamma > 1$, multi-photon ionizations are the dominant phenomena, while if $\gamma < 1$ TI dominates, finally OTBI occurs if $\gamma \ll 1$.

2.1.2 Plasma frequency

In plasma, if electrons are displaced from their equilibrium position while the ions retain their position, an electrostatic field is built due to charge separation, forcing the displaced electrons back to their initial position to restore plasma neutrality. Then, the electrons start oscillating around their equilibrium position with a characteristic frequency know as plasma frequency ω_{pe}:

$$\omega_{pe} = \sqrt{\frac{n_e e^2}{\varepsilon_0 m_e}} \tag{2.3}$$

where n_e is the electron density given in cm^{-3} and ε_0 is the vacuum permittivity.

The dispersion relation for an electromagnetic wave propagating through plasma is given by:

$$\frac{k^2}{\omega_L^2} c^2 = 1 - \frac{\omega_{pe}^2}{\omega_L^2} \tag{2.4}$$

where *k* the wavenumber of the electric field and *c* the speed of light in vacuum, from which the refractive index of the plasma can be derived:

$$n = \sqrt{1 - \frac{\omega_{pe}^2}{\omega_L^2}} \tag{2.5}$$

For electromagnetic waves that $\omega_L \leq \omega_{pe}$, the refractive index becomes imaginary and they can no longer propagate into plasma and thus, they are reflected. Since plasma frequency depends only on the electron density, there is a specific electron density for each wavelength that the electromagnetic wave can no longer propagate into plasma. This critical electron density, is called critical plasma density and is defined by:

$$n_{cr} = \frac{\varepsilon_0 m_e \omega_L^2}{e^2} = \frac{1.1 \times 10^{21}}{\lambda^2 [\mu m^2]} cm^{-3} \tag{2.6}$$

Critical plasma density separates the laser plasma interactions in two regions, namely: a. underdense laser-plasma interaction, where $n_e < n_{cr}$ (electromagnetic waves may propagate thought plasma) and b. overdense laser-plasma interaction, where $n_e > n_{cr}$ (laser cannot propagate thought plasma). The region where it holds that $n_e = n_{cr}$, is called critical plasma surface. For a wavelength value of 800*nm*, the critical density is $n_{cr} = 1.7 \times 10^{21} cm^{-3}$. For laser

intensities above the $10^{18} W/cm^2$ threshold, the laser-plasma interaction becomes relativistic. In that case, the plasma frequency modification is defined by:

$$\omega_{pe_r} = \sqrt{\frac{n_e e^2}{\varepsilon_0 m_e \gamma}} \tag{2.7}$$

and the relativistic refractive index is given by:

$$n_r = \sqrt{1 - \frac{\omega_{pe}^2}{\omega_L^2 \gamma}} = \sqrt{1 - \frac{n_e}{\gamma n_c}} \tag{2.8}$$

where γ is the Lorentz factor and u the particle velocity.

$$\gamma = \frac{1}{\sqrt{1 - \frac{u^2}{c^2}}} \tag{2.9}$$

A fundamental characteristic of plasma is the ability of shielding any external electric potential applied to it. If a charge is applied to a plasma, particles carrying the opposite charge will be attracted to form a sphere around the introduced charge by shielding it, aiming to restore the neutral equilibrium. This sphere has a characteristic screening length, known as Debye length:

$$\lambda_D = \sqrt{\frac{\varepsilon_0 k_B T_e}{n_e e^2}} \tag{2.10}$$

where k_B is the Boltzmann constant and T_e is the electron temperature.

2.1.3 Interaction of a single electron with a laser field

When an electron is implied to the influence of a plane wave, a simple time varying electromagnetic field, it oscillates around a certain position under the influence of the Lorentz force:

$$\frac{dp}{dt} = -e\left(E + \frac{v \times B}{c}\right) \tag{2.11}$$

where p is the electron's momentum, v is the electron velocity and E, B the electric and magnetic field of the laser. This oscillation of the electron is known as quivering motion. The $v \times B$ factor becomes important to the relativistic regime, where the electron velocity approaches the speed of light while in any other case it may be ignored.

A common parameter used to classify the regime of the interaction, is the normalized vector potential:

$$a_0 = \frac{eE_0}{m_e c\omega_L} = \sqrt{\frac{I_L(W/cm^2\ \lambda^2(\mu m^2))}{1.37 \cdot 10^{18}}} \tag{2.12}$$

where E_0 is the maximum amplitude of the laser electric field. Therefore, for $a_0 < 1$ the electron will oscillate linearly along the electric field of the laser.

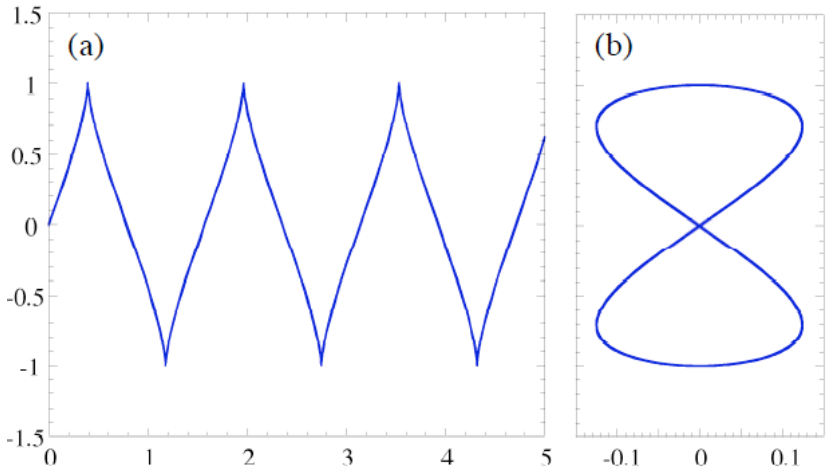

***Figure 2-2*:** (a) Electron motion under electromagnetic wave, (b) the electron 8 figure orbit as viewed from the electron moving frame.

When the electric field is of the order of $10^{18} W/cm^2$, it holds that $a_0 \geq 1$ and the interaction belongs to the relativistic regime. The electron speed approaches the speed of light and the $v \times B$ term cannot be ignored. In this regime, the magnetic field force is acting upon the electron by distorting its trajectory, that now shapes an **8**-figure orbit, as presented at *Figure 2-2*.

2.1.4 Ponderomotive Force

In the case of an electron oscillating under the influence of the Lorentz force of a uniform sinusoidal time varying electric field $E = E_0 \cos(\omega_L t)$ the equation of motion becomes:

$$F = -eE(t), \quad F = a(t)m_e$$
$$a(t) = \frac{dv}{dt} = \frac{-e}{m_e} E_0 \cos(\omega_L t) \tag{2.13}$$

the velocity of the electron is given by integrating acceleration over time:

$$v(t) = \int \frac{-e}{m_e} E_0 \cos(\omega t) dt = \frac{-eE_0}{m_e \omega_L} \sin(\omega_L t) \quad (2.14)$$

The position of the electron is given:

$$x(t) = \int v(t) dt = \frac{eE_0}{m_e \omega_L^2} \cos(\omega_L t) \quad (2.15)$$

where the oscillation velocity of the electron is:

$$v_{osc} = \frac{-eE_o}{m_e \omega_L} \quad (2.16)$$

and the maximum distance from its equilibrium position is:

$$x_{max} = \frac{eE_o}{m_e \omega_L^2} \quad (2.17)$$

In this case the time averaged net force on the electron will be zero, and the electron oscillate around a fixed position, gaining zero kinetic energy.

In a Gaussian profile pulse the Electric field amplitude varies both in space and time and the same holds for the intensity distribution. This results to a higher intensity close to the center of the focal spot while the pulse is been focused. Thus, the time averaged net force on the electron gets a value (≠0), because of the variation electric field amplitude. As a result, the electron does not return at its initial position but drifts away from the focal spot, to regions of lower intensity. Therefore, the electron will be subjected to an averaged net force over the duration of the pulse, known as Ponderomotive Force that is described by:

$$F_p = -\frac{1}{2} \frac{e^2}{m_e \omega^2} \nabla \langle E^2 \rangle = -\frac{1}{2} m_e c^2 \nabla \langle a^2 \rangle \quad (2.18)$$

where $\langle E^2 \rangle$ is the time averaged, squared Electric field and $\langle a^2 \rangle$ the normalized potential vector. The relativistic Ponderomotive Force is derived by equation 2.18 by replacing m_e with the relativistic counterpart γm_e.

2.2 Underdense laser-plasma interaction

2.2.1 Inverse Bremsstrahlung

For moderate laser intensities below $10^{15} W/cm^2$ the dominant laser absorption mechanism is inverse Bremsstrahlung - IB, also known as collisional absorption. During this process, free electrons acquire energy as the laser electric field accelerates them, forcing them to an oscillating

motion. Then the electrons lose their energy through collisions with the ions, coupling this way the lasers energy to the energy of plasma. The absorption coefficient for inverse Bremsstrahlung is:

$$\kappa_{IB} = \frac{Z_i n_e^2}{T_e^{3/2}} \left(1 - \frac{n_e}{n_c}\right)^{-\frac{1}{2}} \tag{2.19}$$

where Z_i is the ion atomic number, therefore inverse Bremsstrahlung absorption is efficient for low electron temperature and high Z_i materials and it can only occur before the plasma critical surface.

2.2.2 Relativistic Self Focusing & Relativistic Critical density

The ponderomotive force of an intense laser pulse ($I > 10^{18} W/cm^2$) expels electrons from a region of high intensity to regions of lower intensity, modifying the electron density and therefore the index of refraction (equation 2.8). The lower electron density to the regions of higher laser intensity results to higher index of refraction, causing a focusing effect to the laser beam propagating through underdense plasma. This focusing effect is known as relativistic self-focusing, in which the laser pulse can overcome diffraction and remain focused for many Rayleigh lengths. Self-focusing will occur for powers over a threshold power given by [23]:

$$P > P_c = 17.3 \frac{n_c}{n_e} GW \tag{2.20}$$

Equation 2.20 denotes that for a laser pulse of 800*nm* wavelength, propagating through plasma with density close to its critical density, the threshold power over which the pulse will undergo relativistic self-focusing, is >3*GW*. This tight focusing of the beam will further increase its intensity.

Plasma critical density (equation 2.6) is the electron density for which the light can no longer propagate in plasma and is reflected. However, for extreme intensities, e.g. a_0>1 where the electron motion becomes relativistic, n_{cr} is modified to:

$$n'_{cr} = \gamma n_{cr} = \frac{\gamma m_e \omega_L^2}{4\pi e^2} \tag{2.21}$$

where $n'_{cr} > n_{cr}$. As a result, extreme intensity laser pulses can propagate further inside an overdense plasma, to greater electron densities, before it gets reflected from its relativistic modified critical density. This effect also known as relativistic transparency.

2.3 Overdense laser-plasma interaction

2.3.1 Resonance absorption

Resonance absorption is a collisionless mechanism, dominant at moderate irradiances $I\lambda^2 \approx 10^{15} Wcm^{-2}\mu m^2$ that couples the laser energy into plasma waves. A p-polarized electromagnetic wave traveling obliquely through a plasma density gradient, will eventually meet the critical surface and will be reflected. The density that the electromagnetic wave gets reflected is lower than the critical density and is given by [25]:

$$n_r = n_{cr} \cos^2 \theta \tag{2.22}$$

where θ is the angle of incidence of the electromagnetic wave k vector to the plasma density gradient. Upon reflection on the n_r density, an electric field component can penetrate through, to the critical density, coupling its energy into a resonant plasma wave, over the critical surface. The plasma wave will deposit its energy in the rest of the plasma, creating a population of electrons with higher temperature than the rest of the plasma electrons. The fraction of the laser energy coupled to plasma via resonance absorption is given by [26]:

$$f_{abs} = \frac{\left(2.3\tau e^{\left(-\frac{2\tau^3}{3}\right)}\right)^2}{2} \tag{2.23}$$

where τ is defined by:

$$\tau = (\omega_L L/c)^{1/3} \sin(\theta) \tag{2.24}$$

where $L \approx c_s \tau_L$ is the plasma scale length, τ_L is the duration of the ionizing pulse and c_s the sound speed in plasma given by:

$$c_s = \sqrt{\frac{Z^* k_B T_e}{m_i}} \tag{2.25}$$

The maximum resonance absorption occurs when $\theta = 45^o$, with the target being normal, while for very small angles or very steep density gradients resonance absorption no longer dominates.

2.3.2 Brunel Effect

The Brunel Effect, also known as vacuum heating, is a heating mechanism firstly conceived by Brunel in 1987 [27]. In the case of intense p-polarized pulse incident obliquely into an overdense plasma with a sharp scale length, comparable to the pulse wavelength, resonant absorption is no longer the dominant heating mechanism and vacuum heating takes place. Electrons from the skin layer of the plasma are extracted into the vacuum region under the electric field of the laser pulse. This results to an electrostatic field due to the charge displacement acting as a capacitor and pulling them back into plasma. As the sign of the laser electric field changes, electrons are accelerated back into plasma because of the laser and the electrostatic field thus, acquiring kinetic energy. As an electron crosses the critical density surface of plasma, is no longer under the influence of the electric field of the laser, since the electric field cannot penetrate plasma. Thus, the oscillation over a certain position will end and the electron will freely stream into the target. The returning velocity of the electrons is given by the oscillation velocity (equation 2.16). When the condition:

$$\frac{\upsilon_{osc}}{\omega_L} > L \tag{2.26}$$

is satisfied, vacuum heating dominates [28]. The efficiency of the vacuum heating mechanism can be up to 70%.

2.3.3 JxB acceleration

Kruer and Estarbrok introduced in 1985 [29] the *JxB* heating mechanism, for laser intensities $I > 10^{18} W/cm^2$ where the electron motion becomes relativistic. As the electron velocity becomes comparable to the speed of light, the *υxB* component of the Lorentz force can no longer be ignored. As electrons oscillate under the influence of the ponderomotive force around the vacuum-plasma interface, they gain energy from the magnetic field, twice per laser circle. This energy, accelerates electrons, streaming them into the overdense plasma, with a frequency of $2\omega_L$. The temperature of the hot electrons accelerated by the *JxB* mechanism has been measured experimentally and computationally [25, 30] and is given by the ponderomotive scaling:

$$T_{hot} = 0.511\left(\sqrt{1+\frac{I_L[W/cm^2]\lambda^2[\mu m^2]}{2.8\ 10^{18}}}-1\right)[MeV] \quad (2.27)$$

2.4 Electron acceleration from solid targets

When an intense femtosecond laser pulse interacts with a foil target of a few μm width, a preplasma is created on the front of the target, induced by the laser prepulse, picoseconds before the arrival of the main pulse. The main pulse interacts with the preplasma, coupling its energy to the plasma electrons by the aforementioned mechanisms, accelerating them to the forward direction through the foil target. These accelerated electrons are called hot electron. After their propagation through the target, the electrons escape into the vacuum, behind the normal of the target, having an opening angle of about 30°. Hot electrons are considered to acquire an exponential energy distribution:

$$n_{hot}(E) = n_o \exp\left(-\frac{E_L}{k_B T_{hot}}\right) \quad (2.28)$$

where n_o is the total electron number, E_L the is the pulse energy given in *J* and $k_B T_{hot}$ the electron temperature based on ponderomotive scaling [31].

An experimental model suggested by Wilks et al [32] estimates the electron temperature to be:

$$k_B T_{hot} \approx m_e c^2\left(1+\frac{2U_p}{m_e c^2}\right)^{1/2} \quad (2.29)$$

where U_p is the ponderomotive potential in *eV* (equation 2.2).

2.5 Ion acceleration

2.5.1 Target normal sheath acceleration

Laser intensities of $10^{24} W/cm^2$ order of magnitude, are required for direct ion acceleration. However, ions can be accelerated indirectly by an electric field, formed from strong charge separation caused from hot electrons that try to escape to vacuum. Several ion acceleration mechanisms have been proposed, each one dominant for different parameters like: laser intensities, target thickness, pulse duration and polarization. One of the most promising ion acceleration mechanisms is TNSA. Early experimental work was reported by E. Clark et al. [33] where ions up to 18*MeV* from the rear of the target had been measured. The experiments were performed using the VULCAN laser at the Rutherford Appleton Laboratory, followed by numerus experiments

reporting ion beam of several 10s of *MeV*s [34,35]. Quasi-monoenergetic ion beams with energy spread less than 20% have been achieved by several groups [36,37] though ion energies did not manage to exceed the 3*MeV*.

TNSA is thoroughly studied, yet not fully understood, and thus experiments and numerical simulations are performed up to date in order to properly understand the acceleration mechanism as well as the laser-target parameters related to it.

2.5.2 TNSA mechanism

As hot electrons leave the plasma, the plasma becomes positively charged, pulling back the less energetic electrons. In the meantime, cold electrons from the bulk of the target act as a return current, rush to shield that abundant positive charge. This shielding prevents further hot electrons to be pulled back or lose energy from the positive plasma. The hot electrons that escaped into the vacuum, form a negative potential also known as sheath which rises in parallel to the target's rear surface. The size of the electron sheath is given by:

$$r_{sh} = r_0 + dtan(\theta_s/2) \tag{2.30}$$

where r_0 is the radius of the laser focal spot, d is the target width and θ_s the electrons sheath broadening angle. Atoms of the contamination layer on the rear surface of the target, most commonly hydrogen, carbon and oxygen atoms [38], are ionized by the huge electric field ~*TV/m* [39]. These ions are therefore accelerated by the electric field of the sheath, being dragged to the vacuum alongside the traveling sheath, propagating parallel to the target normal. Protons have the highest charge to mass ratio, therefore are the particles easily accelerated. The accelerated ions will eventually reach the velocity of the sheath; therefore, the acceleration will stop, and the ions will have acquired their maximum energy. The average energy of the accelerated ions is of the order of few *MeV*'s. A schematic representation of TNSA mechanism is presented in *figure 2-3*.

Passoni and Lontano [40] developed a model based on experimental data, that hold for pulse durations of a few *fs* to almost one *ps* and pulse energies of $\sim 0.1J$ to $\sim 500J$ that predicts the maximum ion energy to be:

$$E_{max} = k_B T_{hot}(4.8 + 0.8\ln(E_L)) \tag{2.31}$$

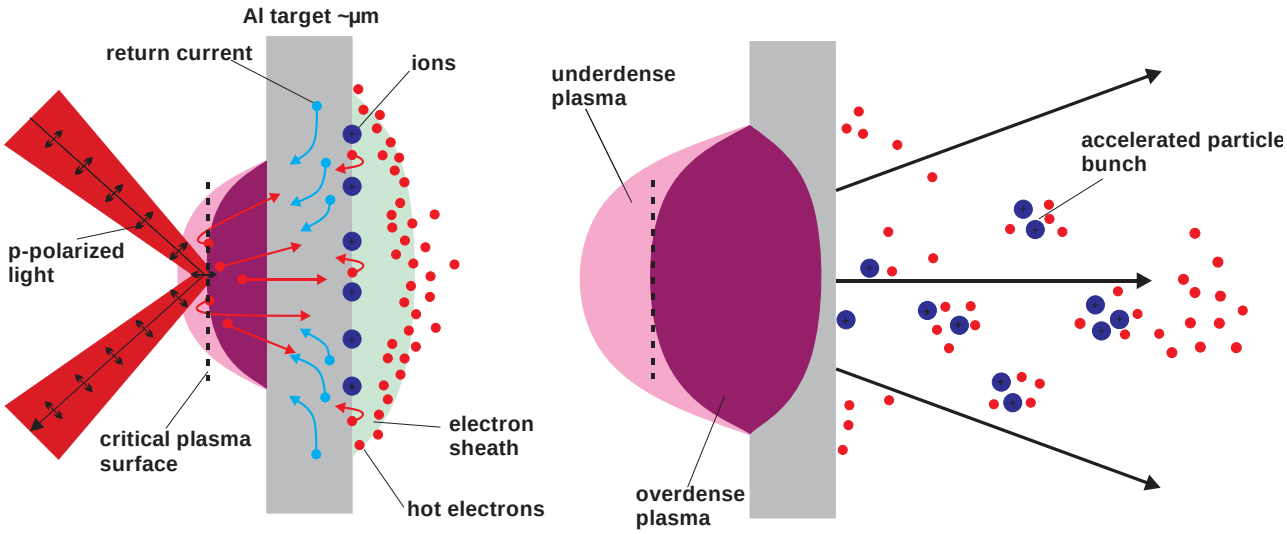

***Figure 2-3*:** TNSA schematic representation. The peak intensity pulse interacts with the formed preplasma. Hot electrons from the critical plasma surface accelerate through the overdense plasma and the foil target while cold electrons rush to shield the abundant positive charge. An electrons sheath is formed to the rear of the target. Ions of the contamination layer are accelerated as the electrons drag them to the vacuum behind the target.

One of the earliest TNSA models was developed by Mora [41]. The isothermal plasma expansion is an analytical model for longer time scales that predicts ion cut off energies given by:

$$E_{max} = 2Zk_BT_e\left(ln\tau + \sqrt{\tau^2+1}\right)^2 \tag{2.32}$$

where $\tau = \omega_{pi}t_{acc}/\sqrt{2\exp(1)}$ is the dimensionless time variable, t_{acc} the ion acceleration time approximately equal to the laser pulse duration and ω_{pi} the ion plasma frequency.

2.6 Ion stopping power

The stopping power of ions is caused by two mechanisms. The electronic stopping power is the loss of projectile ions energy, due to collisions or absorption by bound or free electrons and is the dominant stopping mechanism. The nuclear stopping power describes the loss of energy due to collisions of the ions with the nuclei in the target and it is important only for low particle velocities. The combination of these mechanisms is the total stopping power of the energetic ion propagating inside a medium. The contribution of each stopping mechanism to the total stopping power for protons of 1*KeV* up to 10*MeV* can be observed in *figure 2-4*.

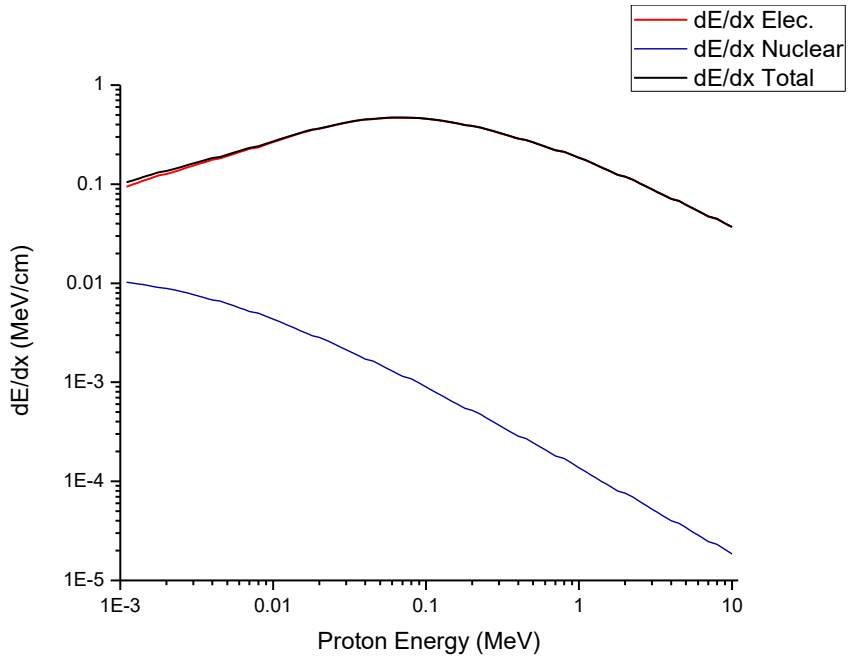

***Figure 2-4*:** Nuclear, electronic and total stopping power for protons from 1*KeV* to 10*MeV* passing through an aluminum medium. The data was accrued using the code SRIM [42].

Bethe [43] formula describes how energetic particles deposit their kinetic energy inside mater and:

$$S_{Bethe} \propto \frac{n_e Z_p^2}{u_p^2} lnf(u_p^2) \tag{2.33}$$

where S_{Bethe} the total stopping power, Z_p, u_p the charge state and velocity of the energetic particle. Since the stopping power is increased linearly with the n_e of the medium, the energetic particles will propagate shorter distance inside materials of greater density. Additionally, the stopping power increase quadratically as the particle velocity decrease, this leads to higher deposition of particle energy, while it slows down. As a result, there is a characteristic peak of energy deposition at the end of the particles trajectory.

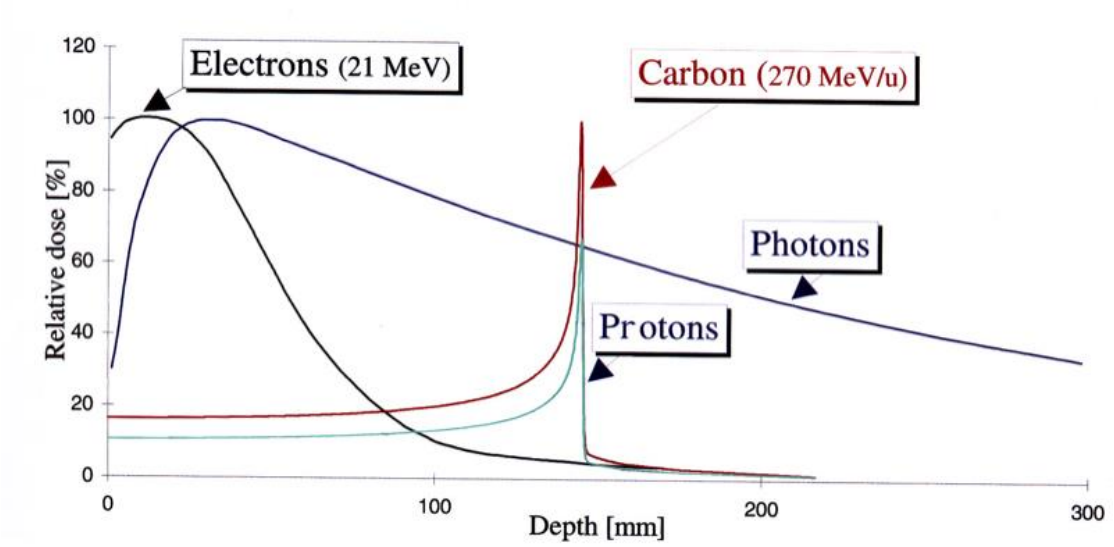

***Figure 2-5*:** Bragg peak of carbon ions and protons compared to how electrons and photons deposit their energy as the propagate through matter.

This peak can be seen in *figure 2-5* of dose deposition as a function of propagated depth of the energetic protons or carbon ions inside matter compared to the way of energy deposition of photons and electrons.

It is clear, that energetic ions can propagate deep into a medium without damaging it along their path and deposit most of their energy to a highly localized spot on the end of their travel, also known as the *Bragg peak.*

Chapter 3

3 Zeus Laser System, Experimental Setup and Diagnostics

3.1 Zeus Laser System

The experiments for this thesis where performed at Zeus laser system, installed at the laboratory facilities of the Institute of Plasma Physics and Lasers - IPPL, located at Rethymnon of Crete. Zeus is an ultra-intense Ti:Sapphire pulsed laser system based on the chirped pulse amplification - CPA technique, introduced by Strickland and Mourou [2] in 1985. Zeus can deliver pulses of 1.2*J* of energy with duration of 25*fs* or higher at a repetition rate of 10*Hz*. The central wavelength of the system is 800*nm*. Each pulse originates from the "Synergy pro" oscillator having energy of few *nJ* and duration of few *fs*. After the oscillator the pulse passes through the contrast ratio booster. There, the pulse energy is amplified by a multi-pass amplifier to a few *mJ*, while a saturable absorber removes a portion of amplified spontaneous emission - ASE of the oscillator, improving the contrast ratio of the pulse (the contrast ratio is discussed at section 3.3). Afterwards the pulse duration is increased from a few *fs* to a few *ps* by a pair of gratings in the stretcher module, reducing this way the pulse intensity, in order to avoid the damage of the optics. After the stretcher, the pulse passes through a sequence of amplifiers, gradually increasing its energy. First is the regenerative amplifier that increases the pulse energy up to 28*mJ*, followed by the first multi-pass amplifier that increase pulse energy to 280*mJ* followed by the final multi-pass amplifier where the pulse is pumped to 1.2*J*. The amplifiers use a Nd:YAG laser with central wavelength of 532*nm*. Finally, the amplified pulse enters the compressor vacuum chamber, where a pair of parallel gratings compresses the pulse to a duration down to 25*fs*.

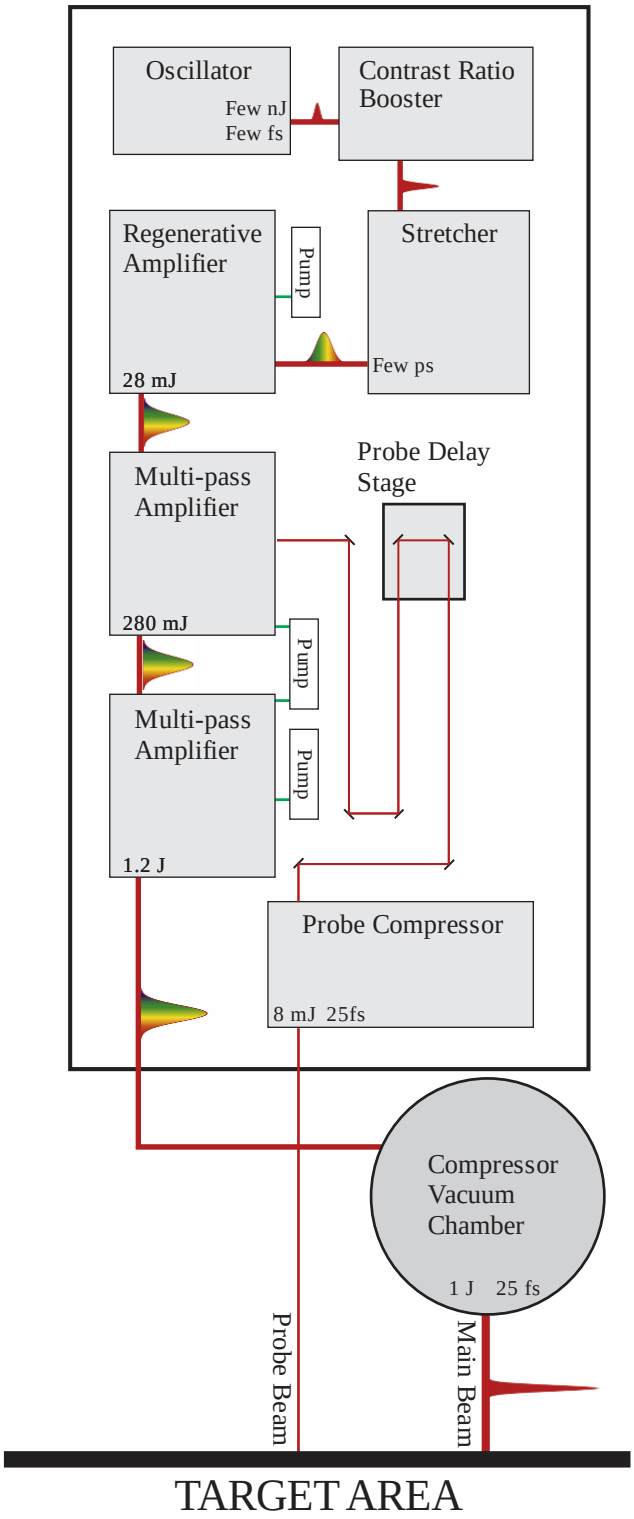

***Figure 3-1*:** Zeus laser set up.

Later on, the pulse is delivered to the vacuum chamber of the experimental facilities. Before the beam enters to the last amplifier, a small fraction of the pulse with 8*mJ* energy is directed through a different root to another compressor and then to the target area. This beam is used as a probe beam for pump-probe experiments. A schematic description of the laser is given in *figure 3-1*.

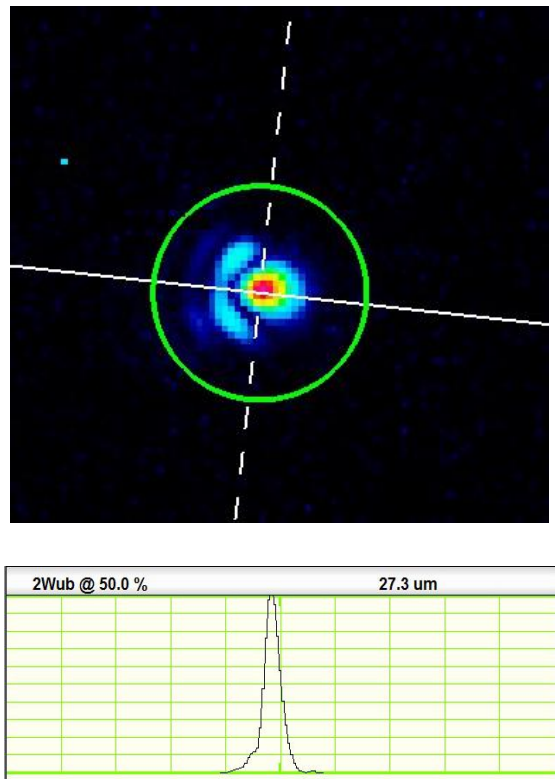

Figure 3-2: The focal spot profile of the Gaussian pulse (up). Spatial profile of the intensity of the pulse, 27.3μm is the diameter of the pulse with magnification x10 at FWHM (down).

3.2 The Target Area

In the target area, a vacuum chamber of $\emptyset$ 1.5*m* is connected to the main pulse compressor vacuum chamber of the laser system. A turbomolecular pump generates vacuum in the order of $10^{-7}mbar$. The main beam enters the vacuum chamber where a gold coated mirror guides it to a 30^{o} off-axis parabola of 15*cm* focal length. The focal spot of the beam was measured and optimized with a profile camera along with a microscope objective with 10 times magnification, found to be 3μm at FWHM resulting to an intensity ~5.7 $10^{20}W/cm^2$ (a_0~16). The beam profile can be seen in *figure*

3-2. A rotation stage, able to hold up to 8 foil targets, was set close to the focal spot. Its micrometric accuracy allowed to focus the beam on the targets.

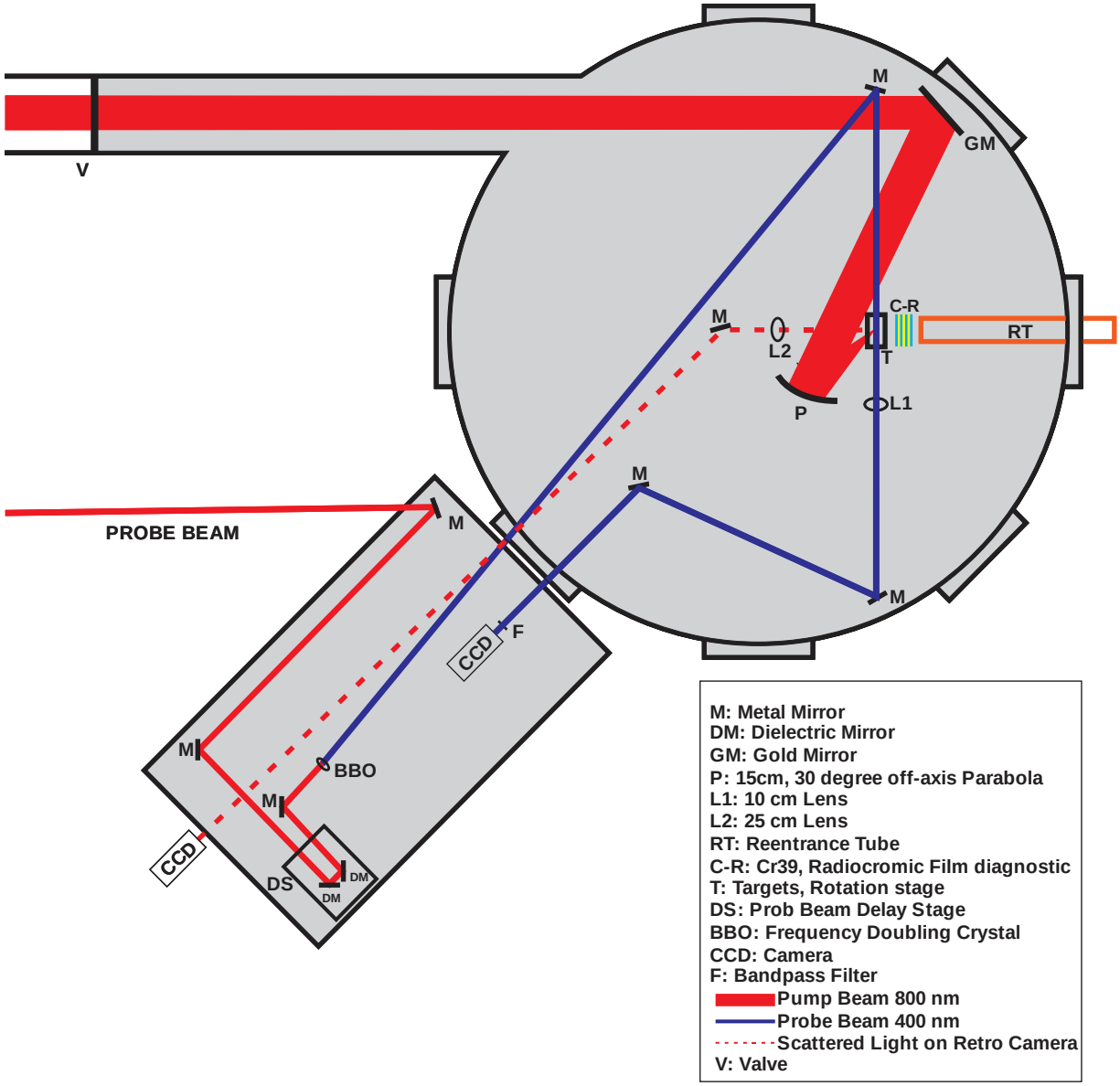

***Figure 3-3*:** The experimental set up in the target area.

The probe beam is synchronized with the main beam using a delay stage, allowing to probe different time frames of the evolution of the experiment. The probe beam is frequency doubled by a Barium Borate crystal - BBO before it enters the vacuum chamber. A sequence of metallic mirrors guides the probe through the interaction spot and again outside of the chamber to the

diagnostic table. While exiting the vacuum chamber, the probe passes through a 400*nm* bandpass filter blocking the infrared scattered light of the main beam. The probe beam ends up to an 8-bit CCD camera used for shadowgraphy diagnostics. A second 8-bit CCD camera is used as a retro-focus imaging diagnostic. The solid target reflects a portion of the laser beam and a small fraction of the reflected light passes through a convex lens and then a metallic mirror sends it to the CCD. Retro-focus imaging allows to monitor the focus quality, while aligning the targets before each shot. The focal spot condition Fon the retro-focus imaging diagnostic can be seen in *figure 3-4.*

Figure 3-4: Focal spot on the retro-focus imaging diagnostic.

To measure the accelerated particles, 2.5*cm* behind the interaction spot a holder is placed for the radiochromic film and the CR39 nuclear track detector diagnostics.

A re-entrance tube was installed to the vacuum chamber, extending 3.5*cm* behind the interaction spot, that allows the irradiation of diagnostics under atmospheric pressure. The re-entrance tube window is made by a 150μm thick plastic film. A detailed description of these diagnostics is given later on this chapter, while a schematic description of the target area is presented in *figure 3-3*.

3.3 Zeus contrast ratio

A crucial laser parameter for the irradiation of solid targets, is the laser system contrast ratio. Contrast ratio is defined as the ratio between the laser pulse peak intensity and the intensity of the laser prepulse. Luminescence from spontaneous emission, amplified to high intensities also known as ASE precedes the main pulse up to a few *ns* ahead. Super intense CPA laser systems suffer from ASE prepulses, with intensities many orders of magnitude below their peak intensity. *Figure 3-5* presents Zeus ASE contrast measured by Amplitudes SEQUOIA autocorrelator. The ASE prepulse

was measured at 450*fs* before the main pulse arrives and the resulting contrast is ~10^7. For pulses of intensity as high as $10^{20} W/cm^2$, seven orders of magnitude lower intensity are enough to heat and ionize the solid target way before the main pulse arrives.

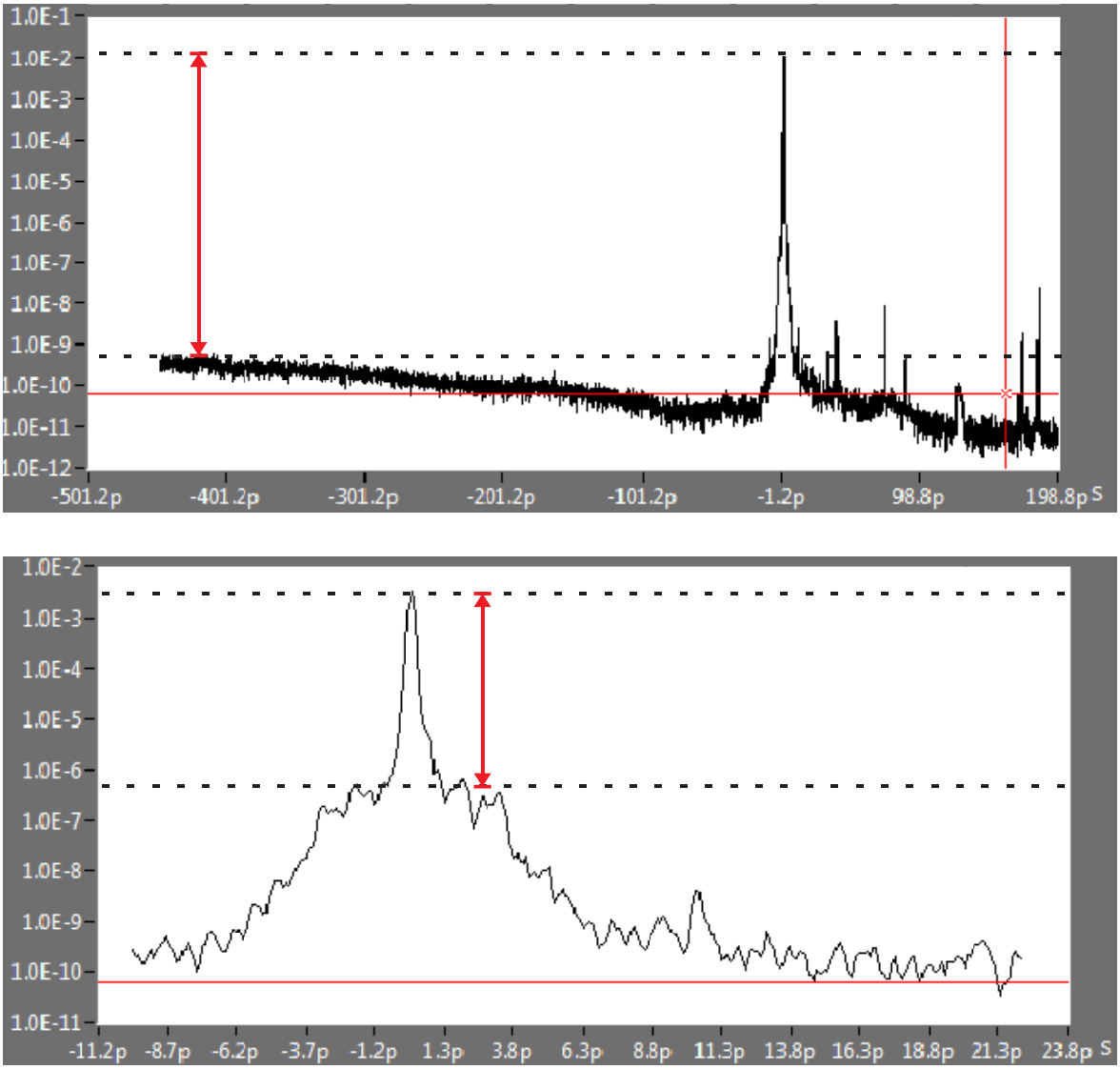

***Figure 3-5*:** ASE laser prepulse at 450*ps* before the peak intensity pulse arrive (up). Prepulse caused by insufficient compression of the pulse prior to the main pulse.

Another important contrast ratio of the laser system comes from insufficient compression of the pulse by the compressor, also known as coherent contrast. Coherent contrast is usually in the *ps* scale and the intensity of this part of the prepulse is higher than ASE. In *Figure 3-5* it may be

observed that the coherent contrast of Zeus laser system is at ~4*ps* before the main pulse arrives with contrast ratio ~10^4.

The laser prepulse can have several effects on a thin foil target before the interaction with the main pulse, such as the deformation of the target's front side, the displacement of the target from the lasers focal position, the creation of long scale length plasma in front of the target affecting the laser focusing conditions of the pulse and generation of a shock inside the target, that will breakout on the rear of the target forming plasma. These phenomena can highly affect the ion acceleration mechanisms [44]. Kaluza et al [45] found that the optimum thickness of a foil target, for ion acceleration varies and is based on the prepulse length as well as on the contrast ratio.

3.4 Diagnostics

3.4.1 CR39 Nuclear track detector

Columbia Resin No.39, also known as CR39, is a transparent plastic polymer allyl diglycol carbonate. It is commonly used as a nuclear track detector [46] and is an ideal detector for measuring ions and protons, while it is not sensitive to electrons, photons and x-rays. When a proton or ion of a certain energy travels through consecutive stacks of CR39 or other materials, if its *Bragg peak* lays to the front or back surface of a CR39, the proton will deliver most of its energy there, causing localized damage and forming a crater or pit. For this pit to become visible, CR39 must be further processed. The irradiated stack must be etched, to do so it is placed into a bath of 30% *w/v* Sodium Hydroxide solution heated to the temperature of 90^o C for 3 hours. This process, dissolves the damaged plastic, broadening this way the size of the formed pits, making them visible to the naked eye. The pits formed by protons will grow to a size of 10μm in diameter while other ions will create larger pits. By placing the etched CR39 under a microscope one can clearly see and count the pits on the surface, if they do not overlap.

For these experiments, a multilayer aluminum mask was attached in the front surface of the CR39. The mask was divided in 8 sectors. The sectors were ranging from 1 to 8 layers of 13 μm aluminum foil resulting to width from 13 to 104μm as shown in *figure 3-6*. The mask is used as a filter of low energy protons. When a proton beam with a broad spectrum of energies passes through the mask, each sector filters out deferent low energy protons. The thinner sector will filter out the lowest energy protons while each consecutive sector will filter increasingly higher energy protons.

Protons with enough energy will pass through the mask and then through the attached CR39. Protons, that their *Bragg peak* lays where the CR39 surface is, will damage its surface. As a result, each CR39 sector is damaged from ions of the same energy. *Figure 3-7* shows the distance a proton can propagate inside Aluminum and CR39 as a function of its energy.

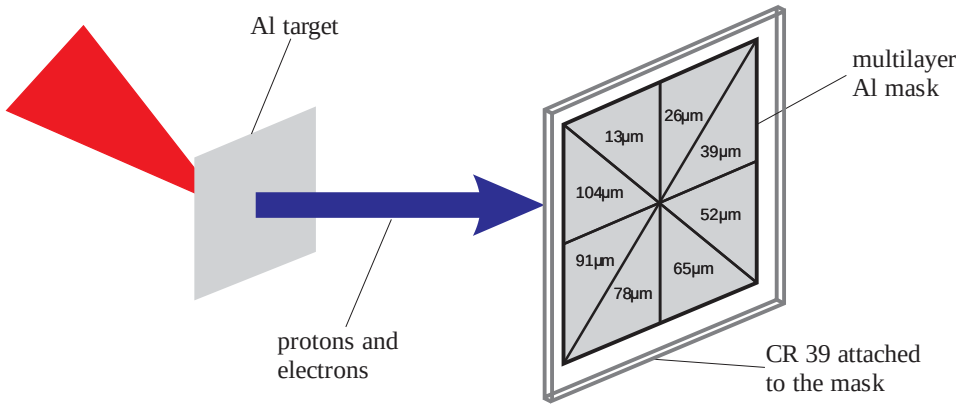

***Figure 3-6*:** Schematic representation of the Al mask – CR39 diagnostic.

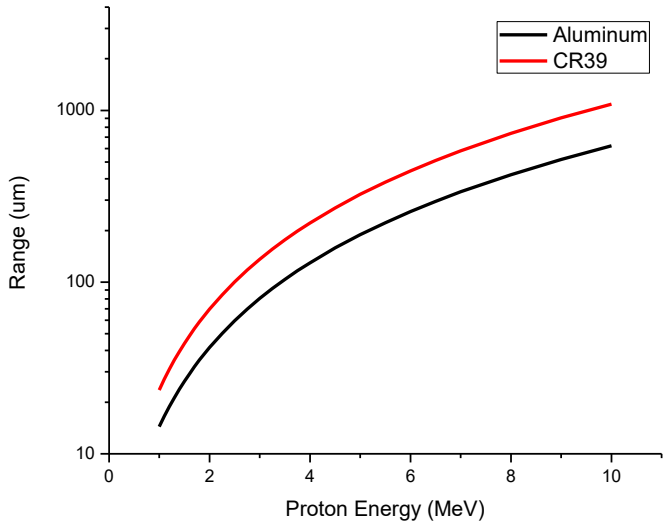

***Figure 3-7*:** Proton traveling range in micrometers inside aluminum for energies from 1 to 10*MeV* inside Aluminum and CR39.

3.4.2 Radiochromic Films

Radiochromic film, also known as RCF is a plastic transparent substrate, coated with an organic die as an active layer. RCF is used to detect electrons, protons, X-rays or any type of ionizing

radiation. When RCF is exposed to ionizing radiation the organic monomer of the active layer undergoes polymerization, leading to change of color from transparent to blue. Higher amounts of ionizing radiation through the film leads to deeper blue colorization. The optical density of the film increases as a function of the absorbed ionizing radiation dose, measured in Gray (*Gy*). By scanning the irradiated films with a reflective 8-bit flat-bed scanner and comparing their optical density with the optical density of pre-calibrated RCF films, the dose on each film can be calculated. The optical density of each film is described by three values of the RGB color code, Red, Green and Blue. By comparing the Blue color pixel value between the irradiated and the calibrated film, the dose can be estimated. The Red and Green color values have marginal impact in comparison to the Blue and can be ignored. The calibration of RCF films is done by exposing films to a ^{60}Co radiation source that emits 1.25MeV photons in a constant rate resulting to a known dosage per hour. A full spectrum of dose can be accrued by exposing different films for different durations to a ^{60}Co radiation source. RCF optical density has an almost linear response to the absorbed dose [47] so a small number of calibrated films is enough to calculate the dose spectrum.

RCF are easy to handle and do not need further processing. About a 90% of the polymerization of the active layer occurs instantly upon irradiation of the film, hence one can read the RCF immediately. The polymerization will be completed after 48 hours, so it is recommended to wait before scanning the RCFs for accurate measurement [48]. RFC responds to all types of ionizing radiation identically, so filters for different kind of radiation must be used to short and identify what will be measured. For this experiment a diagnostic was developed by stacking multiple RCF films covered by a 13μm aluminum filter in order to filter out the electromagnetic radiation, while electrons can pierce through the thin aluminum foil, as presented in *figure 3-8.*

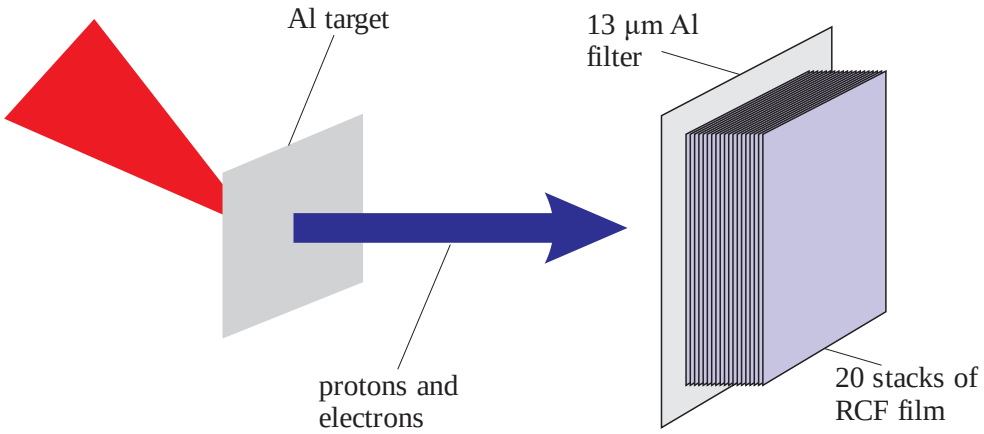

***Figure 3-8*:** The RCF diagnostic for measuring dose from electrons.

The RCF used for this diagnostic is the commercially available Gafchromic HD-810 with thickness about 110μm [50] and can measure up to 400Gy and a calibrated batch of EBT3 [51] films of higher sensitivity and accuracy that can measure up to 20Gy.

Unlike ions and protons way of energy deposition, electrons deposit their energy gradually through their path inside matter as seen in *figure 2-5*. In *figure 3-9* is shown how deep an electron can propagate inside RCF as a function of their energy.

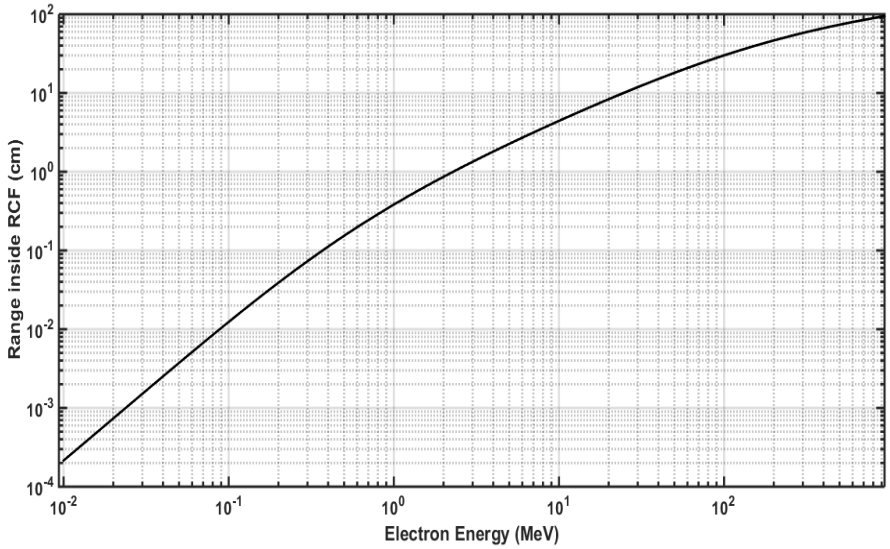

***Figure 3-9*:** The depth inside RCF diagnostic, electrons can propagate based on their kinetic energy, as they gradually deposit their energy through their path.

3.4.3 Shadowgraphy

A very useful probe beam diagnostic, to investigate spatial properties such as the density of the expanding plasma in an intense laser matter interaction experiment, is shadowgraphy. In shadowgraphy the light of the probe beam crosses the main pulse – target interaction area, at a specific time of interest, of the evolution of the interaction. This temporal moment can be tuned by a delay stage enabling us to send the probe beam at later or earlier moments of the interaction. The probing light will pass through a plasma density gradient with non-uniform index of refraction. Light ray passing, through different plasma densities, are refracted at different angles. A CCD camera will gather the refracted light along with the unperturbed light that traveled through the vacuum. Therefore, variations on the brightness of the image indicate variations in the plasma density. The darker regions of the image correspond to higher density regions of the plasma. If the plasma density is locally above the probe beams critical density, dark regions will appear in the image, as is schematically depicted in f*igure 3-10*. Shadowgraphy is a great diagnostic to acquire qualitative data about the shape, size and density gradient of plasma [49].

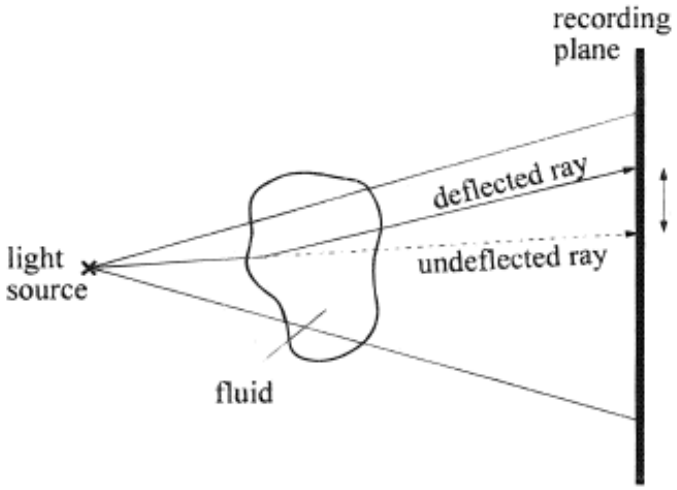

Figure 3-10: Principles of shadowgraphy.

Chapter 4

4 Experimental results

In this chapter, the measurements of energetic protons and electrons form the interaction of Zeus laser pulse with micrometric solid target, are presented. For these experiments the targets that were used were Aluminum foils of 1.5, 5, 13 ,30 and 70μm. The energy of the beam at the target area (after the compressor) was measured to be 1J, focused in a 3μm diameter FWHM, while the pulse duration was varied from 25fs up to 150fs. For each experiment 8 shots were performed. This limitation was due to the maximum of 8 targets that could be mounted in the target rotation stage. After that the vacuum chamber was atmosphere in order to mount new foil targets.

During these experiments, it was realized that the altering of target thickness and pulse duration did not have the expected results and that the particle cut off energies were not as high as expected. This problem was countered due to the laser's low contrast ratio and the early preplasma formation that disrupts the TNSA mechanism.

In the first section the results of accelerated protons are presented, while in the second section the electron measurements are presented.

4.1 Energetic proton measurements

During this experiment a parameter scan was performed altering target thickness and pulse duration in order to study the effects on the particle beam. Many parameter combinations resulted to non-measurable protons, or protons of energy below 400keV, that is the sensitivity of the CR39 diagnostic. In *figure 4-1* the highest proton energies from the possible parameter combinations on the CR39 nuclear track detector diagnostic, are presented.

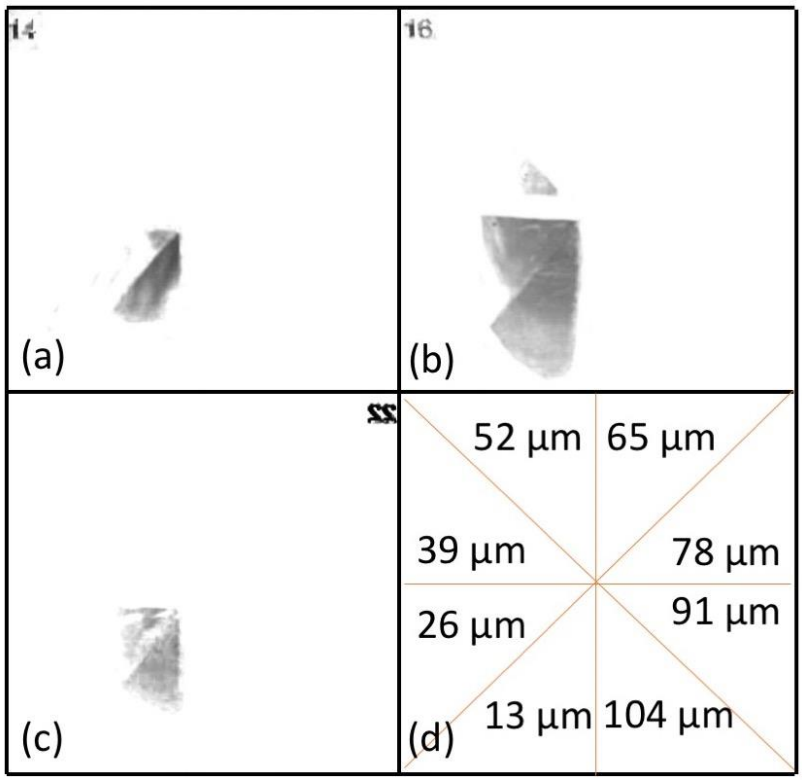

***Figure 4-1*:** The scanned CR39 of the shots with the best results. (a) 70μm aluminum target irradiated by 25fs pulse with cut off proton energy 1.5MeV. (b) 30μm aluminum target, 80fs pulse, cut off proton energy 2MeV. (c) 30μm aluminum target, 150fs pulse, cut off proton energy 1.5MeV. (d) Schematic representation of the thicknesses of the different sectors of the aluminum filter mask.

Case (a) corresponds to 8 shots on a 70μm Al foil, with pulse duration of 25fs. Measurable protons appear in two sectors of the CR39. The protons were able to propagate up to 26μm inside aluminum, which according to *figure 3-6* corresponds to proton energies of 1.5MeV. In case (b) the target was 30μm Al foil and the pulse duration was set to 80fs. Here the proton signal appears in 3 sectors. The high energy protons had a *Bragg peak* on 39μm inside the aluminum which corresponds to proton energy of 2MeV. In case (c), the target was again 30μm aluminum and the pulse duration was set to 150fs resulting in a cut off proton energy of 1.5MeV. Lower number of 1.5MeV protons was also measured for 30μm target interacting with 25fs pulse and 70μm target interacting with an 80fs pulse, while it is worth mentioning that for 1.5 and 5μm foil targets there were no measurable proton signals on the CR39. These very thin targets were destroyed, long before the peak intensity pulse arrival, unlike the thicker targets. The optimum target thickness for

target normal sheath acceleration with a pulse of contrast of the order of ~10^7 was found to be the 30μm thick aluminum foil.

Due to high proton flux, CR39 were saturated close to the center, denoting that the pits formed during the etching prosses, were overlapping. For the CR 39 of the case (b), a region of about 0.5cm far from the center, was chosen to count their relative proton surface density. These measurements were performed by counting pits on the surface area of 100 x 100μm of the CR39, using a microscope objective x25 magnification. They are presented in *figure 4-2*, although the number of pits in the saturated area were much higher.

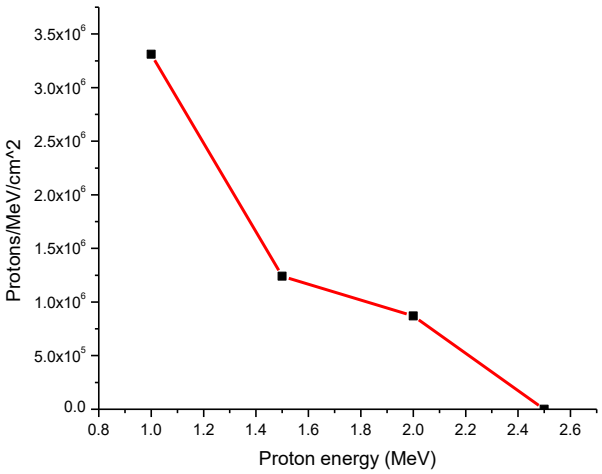

***Figure 4-2*:** Protons/($MeVcm^2$) as a function of their energy counted in the CR39 surface from 30μm Aluminum target irradiated by 80fs pulse.

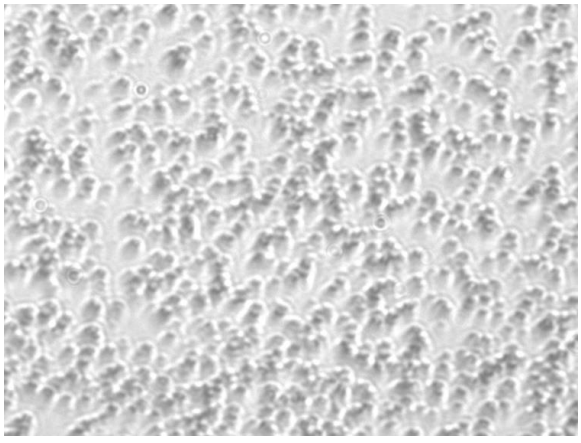

***Figure 4-3*:** Pits on the surface of an etched CR39 in a non-saturated area.

The value of the portion Protons/cm^2 is of the order of 10^6, indicating that these protons correspond to the tail end of the energy spectrum, while the majority of the accelerated protons energy were below 1*MeV*, where the diagnostic was not able to measure. In *figure 4-3* the pits on the surface of the case (b) CR 39 in the lower energy sector are depicted. The pit size was measured to be about 11μm, formed from protons. Other type of ions creates larger pits on CR39, though no such pits were observed, meaning that only protons were accelerated [16].

Higher energy proton beams are more collimated, as can be observed in *figure 4-4*, where the proton beam opening angle relative to the beam propagation direction, is presented as a function of the beam proton energy. The Profiles of the proton beams of 1 and 1.5*MeV* energies form a 30μm target are depicted in *figure 4-5*.

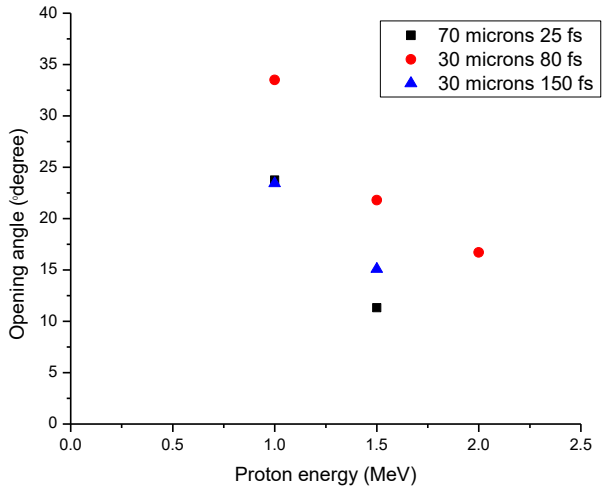

***Figure 4-4*:** Opening angles of the protons as a function of their kinetic energy for the CR39 shown in figure 4-1.

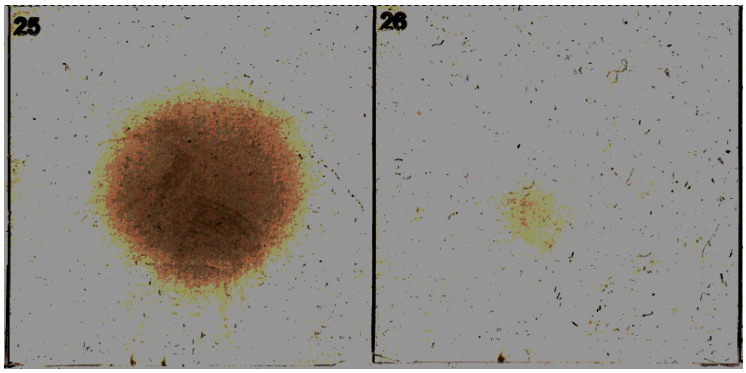

***Figure 4-5*:** Profile of the proton beams of 1 and 1.5*MeV* energies form a 30μm target, after brightness and contrast adjusting in order to highlight their features.

4.2 Energetic electron measurements.

A stack of 20 RCF HD-810 films were used to measure the electron dose generated by the irradiation of a10μm thick aluminum foil, by 8 shots. The resulting dose is demonstrated in *figure 4-6*. Below the irradiated RCF films are the pre-calibrated RCF by the ^{60}Co radiation source presented.

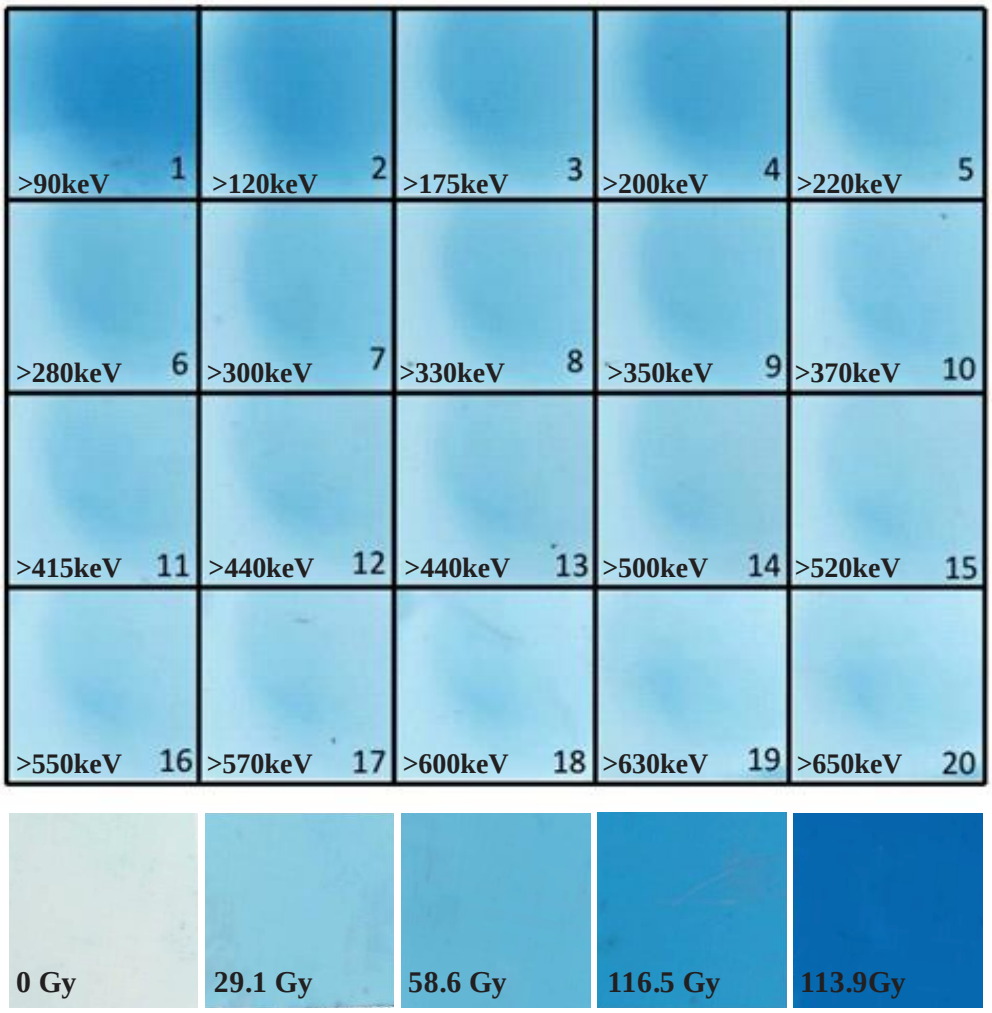

***Figure 4-6*:** The dose on the 20 consecutive RCF films. On each film the minimum energy that can penetrate up to its depth appears. Below, the calibrated RCF films with their corresponding doses.

The RCF stacks where covered with 13μm aluminum foil, in order to filter out the IR light from the laser beam and the dose of the protons of energy up to 1MeV. Higher energy protons may have deposited dose in only the first RCF film, since their Bragg peak is less than 40μm inside RCF,

while each RFC has a thickness value over the 100μm. Since the RCF optical density response to dose is almost linear, the intermediate dose values can be found by interpolation of the optical density response to dose. Each value of the blue channel (0-255) of the RGB scale corresponds to a specific dose. The total dose, of the 8 shots as a function of depth, is plotted in *figure 4-7* ranging from ~120*Gy* for the first film down to ~8*Gy* for the last. Since 8 shots were performed during the experiment, this results to ~15*Gy/shot* down to ~1*Gy/shot* for the most energetic electrons.

Since electrons of specific energy propagate up to a certain distance, each subsequent RCF film has received dose of electrons of a threshold of the minimum energy and above and all films before that, act like the lower electron energy filters. The minimum electron energy that deposited dose for each RCF is presented in *figure 4-6*.

The number of electrons/cm^2, required to deliver a particular dose, can be estimated by:

$$\Xi(elctrons/cm^2) = \frac{p[kg/cm^3]}{E[MeV] \times 1.602 * 10^{-13}} \times Dose[Gy] \tag{3.3}$$

where $p = 1.29 * 10^{-6}\ kg/cm^3$ is the density of dry air and E the energy of the incident electrons. Since the last RCF film showed ~8*Gy* of ionizing radiation of ~0.6*MeV* electrons out of 8 shots in total, this means that each shot accelerated ~1.3x10^7 *elections/cm*^{2}.

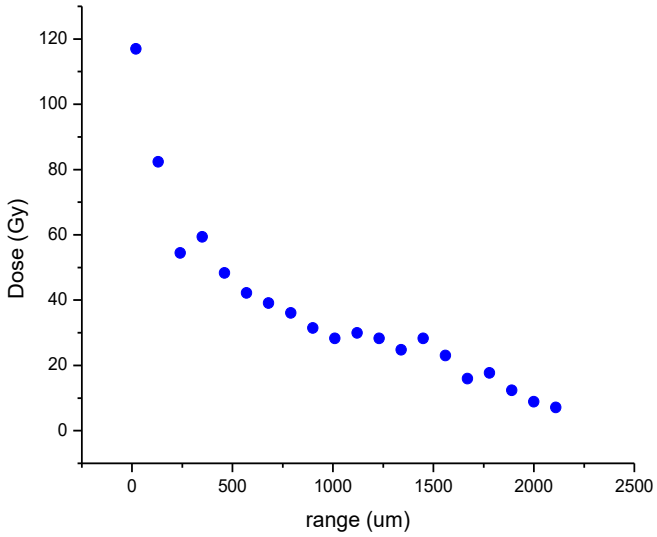

***Figure 4-7*:** Dose from electron ionizing radiation as a function of depth inside RCF integrated over 8 shots.

To measure the dose inside the re-entrance tube, where samples can be irradiated under atmospheric pressure, a stack of EBT3 calibrated RCF films by RTsafe [51] were used. For this measurement 20 shots on 30μm thick aluminum were performed. In this case the dose of ions was filtered out by the ~150μm plastic window of the Reentrance tube alongside with 13μm Al photon filter. The RCF films where scanned by an EPSON V850 Pro scanner. *Figure 4-8* presents the electrons dose profile on the irradiated film and a lineout of the dose.

The electron dose of ~20Gy out of 20 shots is sufficiently less than the dose on HD-810 films taken by 8 shots, due to the electrons losing a fraction of their energy while they propagate through the window.

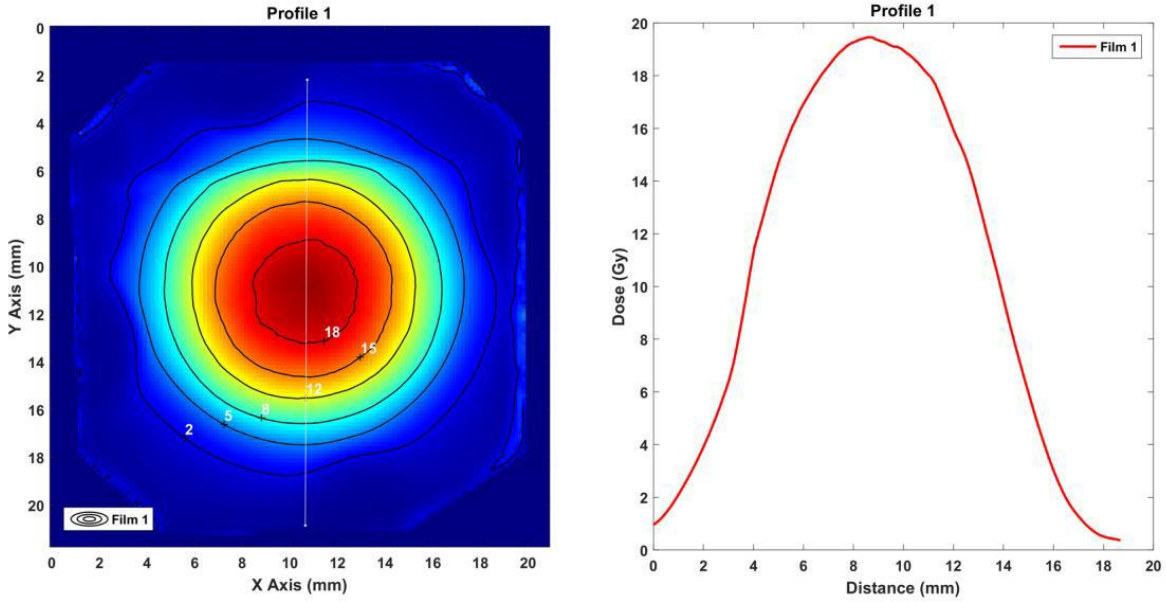

***Figure 4-8*:** Electron dose profile of the EBT3 RCF films irradiated by 20 shots inside the re-entrance tube, the ring appearing on the profile are isodose lines. At right, a line out of the dose as a function of distance.

4.3 Shadowgraphy diagnostic results

Shadowgraphic imaging provided qualitative information of the target conditions, before the arrival of the main pulse. Preplasma expansion appears in the rear of the target, 1ps before the high intensity part of the laser pulse, as seen in *figure 4-9*. The target thickness is 30μm while the critical density of the plasma has extended up to ~5μm. This preplasma was generated by the ASE prepulse

and the inefficient compression of the pulse ramp, heating and possibly sending a shock inside the target that leads to deformation and early ionization of the target.

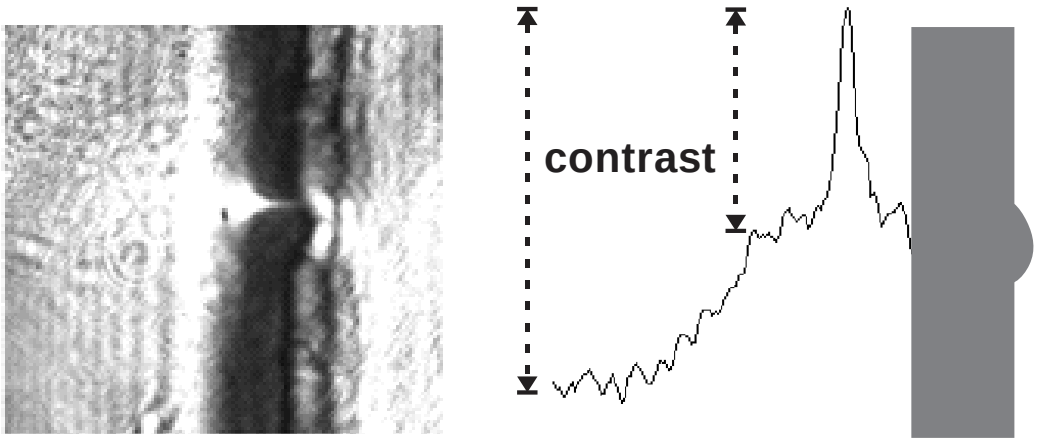

***Figure 4-9*:** Shadowgraphic image of the interaction of the 30 μm aluminum target 1*ps* before the main pulse arrives (right). A schematic representation of the intensity of the pulse 1*ps* before the peak internist arrive the target.

The bright region in front of the target is caused by harmonic generation during the interaction of the pulse with the solid target [52]. 400*nm* bandpass filter placed at the exiting window of the probe does not block the light of the second harmonic. As a result, the preplasma expansion in the front of the target is obscured in the shadowgraph. Although the existence is of a few μm, sharp gradient density preplasma is crucial both for the Brunel effect and the focusing conditions of the main beam.

Chapter 5

5 Particle in cell simulation

In order to further understand the experimental results, as well as to study the effects of the laser's inherent ASE prepulse on the TNSA mechanism, numerical particle-in-cell – PIC simulations were performed. These simulations were performed using the EPOCH relativistic PIC code [53].

EPOCH initially calculates the electric and magnetic field values on the grid., by solving the Maxwell equations At the next step the velocity of the particles is calculated and their new position on the grid is updated, by solving the Lorentz equation. Finally, the current density from the particle flux, through the grid is calculated, which in turn affects the electric and magnetic fields on the grid. After a full iteration these steps are repeated, as it is schematically shown in the flowchart of *figure 5-1*.

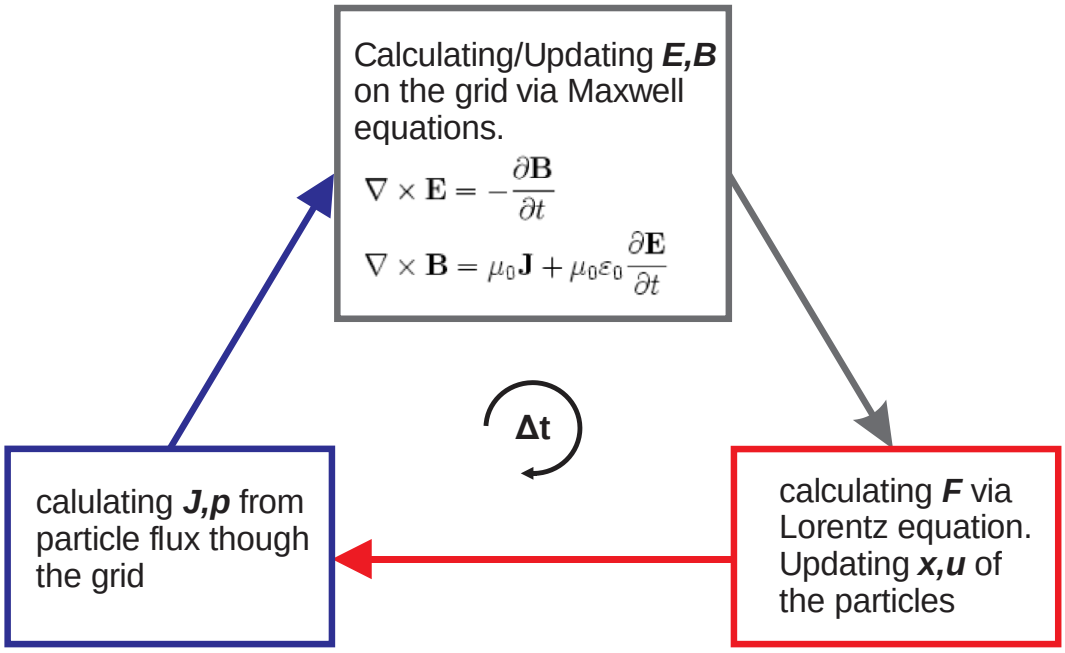

***Figure 5-1*:** The particle-in-cell scheme. The steps of one full iteration.

During the pre-processing of a simulation, numerous parameters and limitations must be taken into account. The dimensions of the simulation are chosen. EPOCH allows for 1,2 and 3D simulations, while the more the dimensions used, the higher the computational demands are. Then, the

simulation solution domain (box size) and the duration are set, based on the interaction time of interest. The spatial resolution of the simulation comes from the chosen grid points that divide the simulation box into cells. The cell size should meet certain criteria, e.g.: if the cell size exceeds the Debye length of the simulated plasma, nonphysical electric fields will arise on the grid, leading to rapid increase of the particle energy. This issue is known as numerical heating. EPOCH uses macroparticles which represent many real particles, acting collectively. This division of actual particles into less macroparticles relaxes the computational demands of a simulation, although a very low number of macroparticles will lead to unnatural heating of the plasma. The electron temperature should be also taken into consideration. For higher electron temperatures the Debye length increases in size and this relaxes the spatial discretization requirements in order to resolve it although one should be careful not to excide the actual temperatures the electrons would acquire from a real laser prepulse. Additionally, unnaturally high electron temperature will lead to unreal plasma expansion rate. If λ_D is resolved, the time step must be

$$\Delta t \leq \frac{1}{c\sqrt{\left(\frac{1}{\Delta x^2}+\frac{1}{\Delta y^2}\right)}} \tag{5.1}$$

to preserve the numerical stability.

5.1 PIC simulations on High Performance Computers

PIC simulations are extreme computational demanding, due to the need of resolving many spatial scales down, to *nm* levels, while the number of macroparticles involved in the simulations may often be in the order of 10^9. Memory requirements can go up to 100's of GB of RAM per simulation, while the output SDF files sizes, may preserve tens of GB's. As a result, PIC simulations are usually unable to run in conventional PC's or Clusters. PIC simulations are usually performed in High Performance Computers (HCP's). Parallelization is the splitting of a problem into discrete parts that can be solved simultaneously in different processors, also known as problem decomposition. The PIC simulations performed in this Thesis, were performed with computational time granted from the Greek Research & Technology Network (GRNET) in the National HCP facility of GRNET HPC-ARIS. The 2D simulations were performed using the opensource advance relativistic EM MPI parallelized code EPOCH. Up to 700 cores (35 nodes with 20 cores each)

were used for each run. Prior to the actual simulations, a scaling performance study was performed, to determine the optimal number of cores required for these PIC simulations.

Initially, a benchmark simulation with a solution domain of size of 20 x 40μm and a cell size of 20x20nm using 10^7 macroparticles was performed, on 20, 40, 60, 80, 100, 200, 300, 400, 500, 600 and 700 computer cores. The simulation time of the interaction was set to 250fs. In *figure 5-2* the duration of the simulations in minutes as a function of the number of the cores used is presented. In *figure 5-3* the core-hours consumed for each simulation are depicted. The speed-up percentage of each consecutive run vs the reference run (of 20 cores) is demonstrated in *figure 5-4.* It may be observed that beyond the 300 cores, a plateau appears.

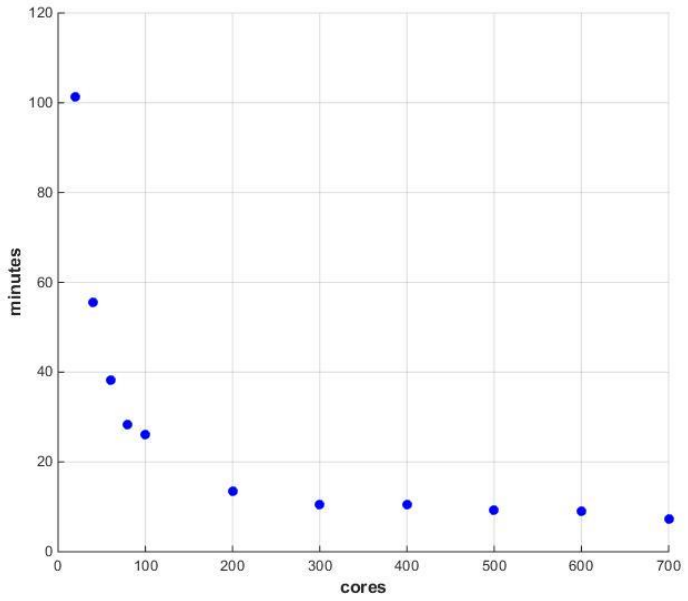

***Figure 5-2*:** Simulation duration as a function of cores used for the first scaling scenario.

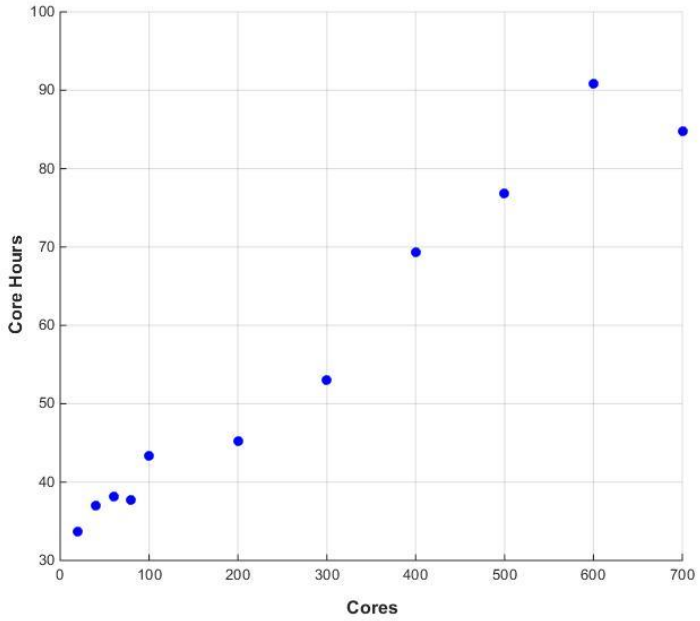

***Figure 5-3*:** Core-hours spent for each run of the first scaling scenario as a function of cores used.

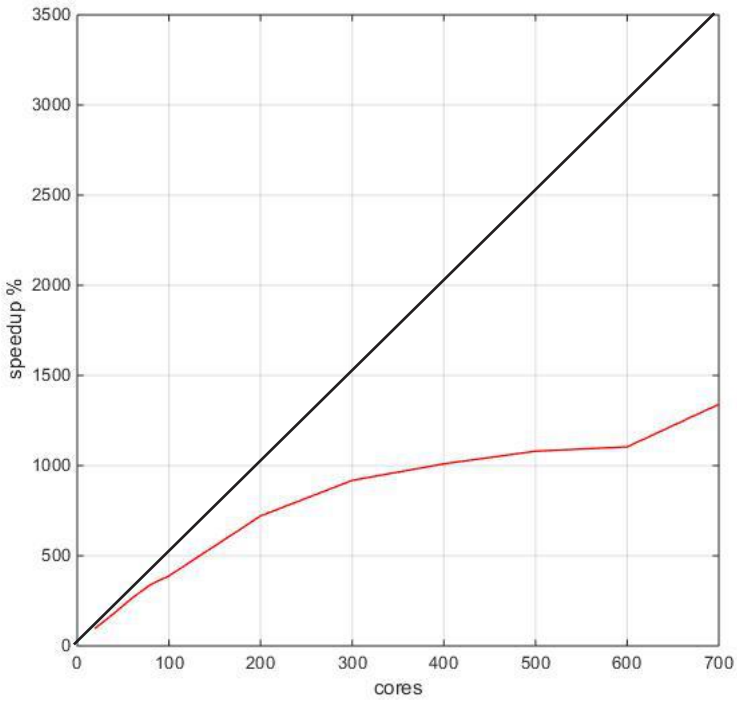

***Figure 5-4*:** Speedup percentage of each consecutive run vs the reference run (20 cores).

Further scaling tests were performed for the study of the multiprocessing efficiency for even higher demanding simulations. A 20 x 40μm domain discretized by 2 x 2nm cells with a 25fs simulation time and a number of macroparticles of 10^9, was set. The run-time in minutes, as a function of the cores used is presented in *figure 5-5*, while the speed-up percentage of each consecutive run vs the reference run (of 100 cores), is demonstrated in *figure 5-6*. In this case the multiprocessing was efficiently scaled-up to 600 cores.

Based on the scaling tests, the optimal number of cores was determined to be in the range of 400 to 600, having a run time of 24-70 hours that results to ~15.000 - ~42.000 core-hours).

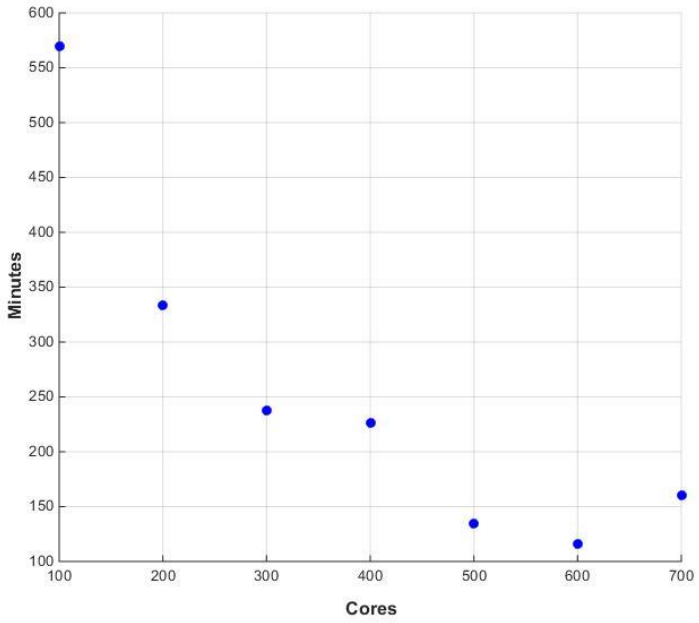

***Figure 5-5*:** Simulation duration as a function of used cores for the second scaling scenario.

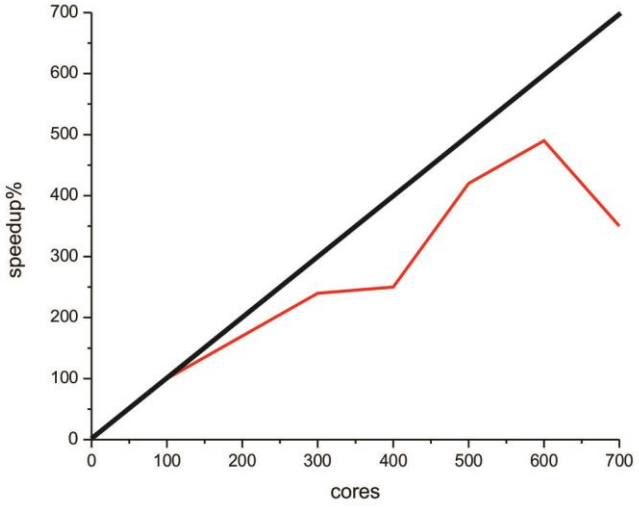

***Figure 5-6*:** Speedup percentage of each consecutive run vs the reference run (100 cores).

5.2 PIC simulation set up

An overdense pre-ionized hydrogen plasma, was chosen to simulate the solid density Al targets. Two main scenarios were considered. The first corresponds to a simple ionized hydrogen column, that simulates a clear interaction, with no preplasma expansion. This scenario may stand for laser systems of high contrast ratio ($>10^{10}$). For the second scenario, a ramp of exponentially decreasing plasma density e.g. see [54], varying from the initial target density down to zero, in a distance of $20\mu m$, expands in front and rear of the hydrogen plasma target. The critical plasma density on the front side is at distance of $7\mu m$ from the target and at $5\mu m$ distance at the rear of the target. This density gradient is used to model the preplasma effect of the prepulse of the laser system. This 2nd scenario, was based on the experimental observations of plasma expansion on the rear of the target, at 1*ps* before the pulse peak intensity arrives. In f*igure 5-7*, the modeled target at t=0 of the simulation, is presented.

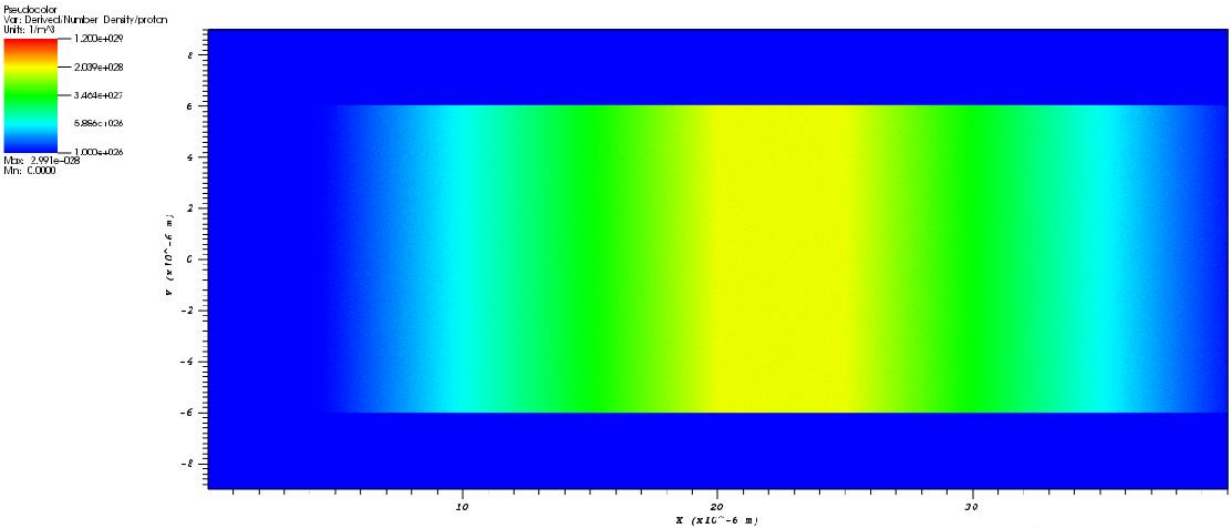

***Figure 5-7*:** The 5μm target with preplasma expanding in front and rear of the target at t=0.

A parametric scan was performed for the study of the dependence of the proton cut off energies on target thickness to the pulse duration. The simulated targets were chosen to be 5μm, 10μm and 30μm, while pulse durations of 25fs and 80fs were selected. Each one of the two sets of parameters were tested for both of the scenarios. The simulation boxes were set to 20 x 18μm for the 5μm targets and then varied, based on the size of the target, up to 65 x 18μm for the 30μm target with preplasma expansion. The total simulation time was 250fs. The target density was set to be $n = 10n_c$ and the electron temperature T_e=1000eV thus, resulting to a Debye length of $\lambda_D = 2nm$ and proton temperature of T_p=100eV. The number of grid points was set, so as the cell size to be 2 x 2nm, in order to resolve the λ_D. For the 30μm targets, the cell size was chosen to be 2 x 4nm in order to relax the computational demands of the simulations. The time step was $\Delta t = 0.0045 fs$ with some variations based on the number of grid points of each simulation. The time step requirement for numerical stability was resolved. The total number of macroparticles was 10^9. The laser was initialized at the left side of the box, propagating along the X-axis, perpendicular to the target normal. The rest boundaries where set to be open. The laser pulse was set to be of a Gaussian profile, with main wavelength of λ=800nm, of p-polarization, with a focal spot of 3μm at FWHM resulting to an intensity of 5.7 $10^{20} W/cm^2$ ($a_0 = 16$) for 25fs pulse duration.

5.3 PIC simulation results and analysis

In f*igure 5-8 up*, the Electric field of the laser beam as it focuses on the target is presented, while the fully build electron sheath is demonstrated *down*. The Electrostatic field of the sheath is of the order of magnitude of the laser pulse electric field ~10^{12}*V/m* -10^{13}*V/m*.

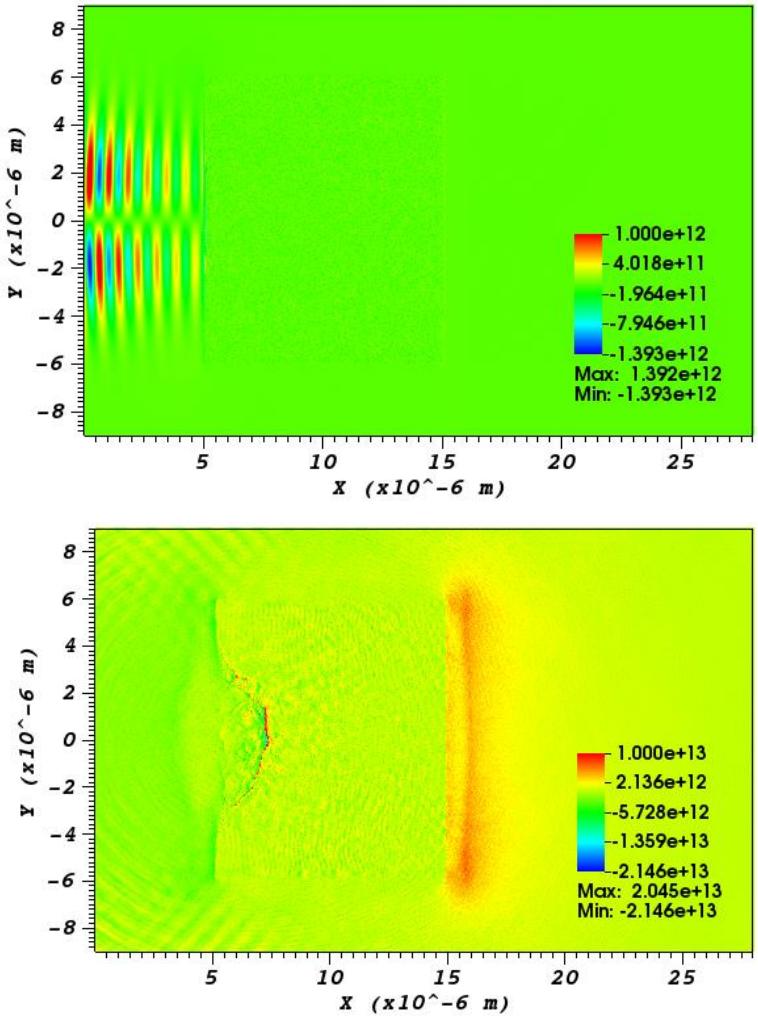

***Figure 5-8*:** (up) The electric field of the laser pulse at simulation time 25*fs*, (down) evolution of the electric field of the fully build up sheath at simulation time 125*fs*.

The interaction of the 5μm target with no preplasma expansion, at 250fs of the simulation, is presented in *Figure 5-9*. All figures are plotted in logarithmic scale in order to emphasize the low-density regions.

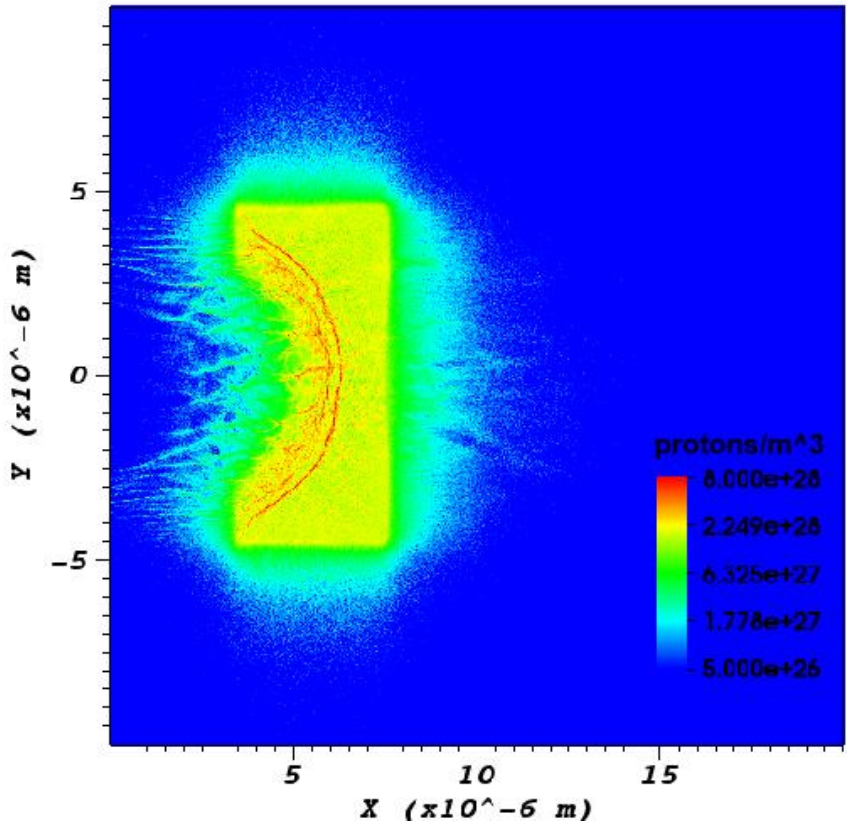

***Figure 5-9*:** Protons pseudocolor logarithmic plot of the 5μm target without preplasma expansion, interacting with 25fs pulse, at t=250fs of the simulation.

It can be observed that the critical plasma surface is pushed back and into the target, by the laser pulse. This indicates that more than one acceleration mechanisms take place on the interaction. The first mechanism is the TNSA, that accelerates protons through charge separation in the rear of the target. The second mechanism, is the proton acceleration by a collisionless electrostatics shock wave, formed at the front of the target [17][55][56]. In such high laser intensities, the radiation pressure of the laser can overcome the thermal pressure of the plasma, pushing the electrons of the plasma backwards and forming a steep gradient electron density that will accelerate protons on its wake, as it propagates through the target, described by:

$$P_R = 2I_L/c \tag{5.2}$$

In *figure 5-9,* the preceding fine structure of high density shows the protons accelerated by this type of shock. This shock may propagate having a velocity of multiple times of the sound speed of plasma (see equation 2.25). Since T_e is high, due to the intense heating of the electrons by the focused pulse, c_s/c can exceed the value of 0.1 (for $1MeV$ electrons $c_s \approx 1 * 10^7 m/s$). In this simulation the shock front velocity reached the value of ~1.1 $10^7 m/s$. The maximum velocity that an ion can reach by that mechanism, is twice higher the velocity of the shock, which is acquired by the ions reflected by the shock's front. The fine structure closer to the focal spot of the laser, in *figure 5-9,* is a second electrostatic shock of lower density, that reaches to a slightly higher velocity, with a max value of 1.2 $10^7 m/s$. This can be explained by considering that as the intensity of the pulse rumps up, the second shock was created by a following part of the pulse having an even greater intensity.

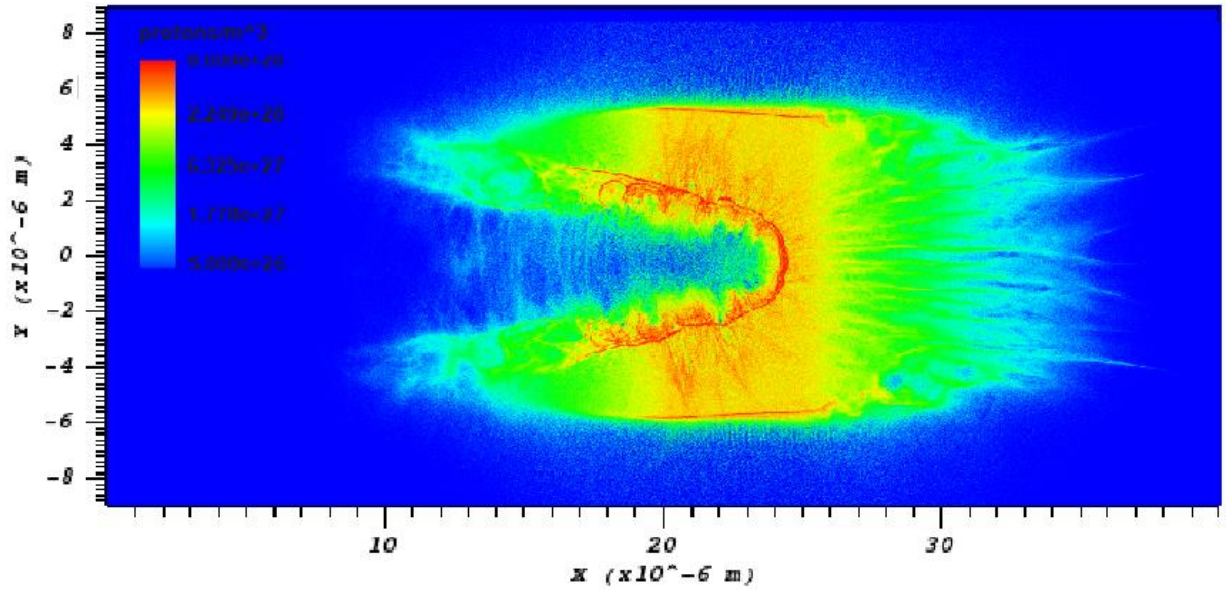

***Figure 5-10*:** Protons pseudocolor logarithmic plot of the 5μm target with front and rear preplasma expansion, interacting with 25fs pulse, at t=250fs of the simulation.

In ICF, the compression of the target is driven by shock waves. Strong shock waves produce a large amount of entropy. In order to avoid this, instead of sending one strong shock, a specially tailored beam generates a high number of weaker shocks, where each shock of the sequence has a higher velocity than the predecessor. As a result, these shocks superimpose to a strong shock [57]. The same shock velocities were observed for the 10μm and 30μm targets. The width of the structures was found to be ~1.18μm, comparable to that size of the wavelength of the laser.

In *figure 5-10*, is presented the preplasma expansion scenario for the 5μm target. It is noticeable that the laser beam is more tightly focused that the no-preplasma counterpart, and this is a result of relativistic self-focusing. According to equation 2.20 for the electron density in front of the pulse (~2.5 10^{27} m^{-3}) the P_c has a value of 11.76*GW*, so the power of the laser beam is way above the threshold power under which self-focusing occurs.

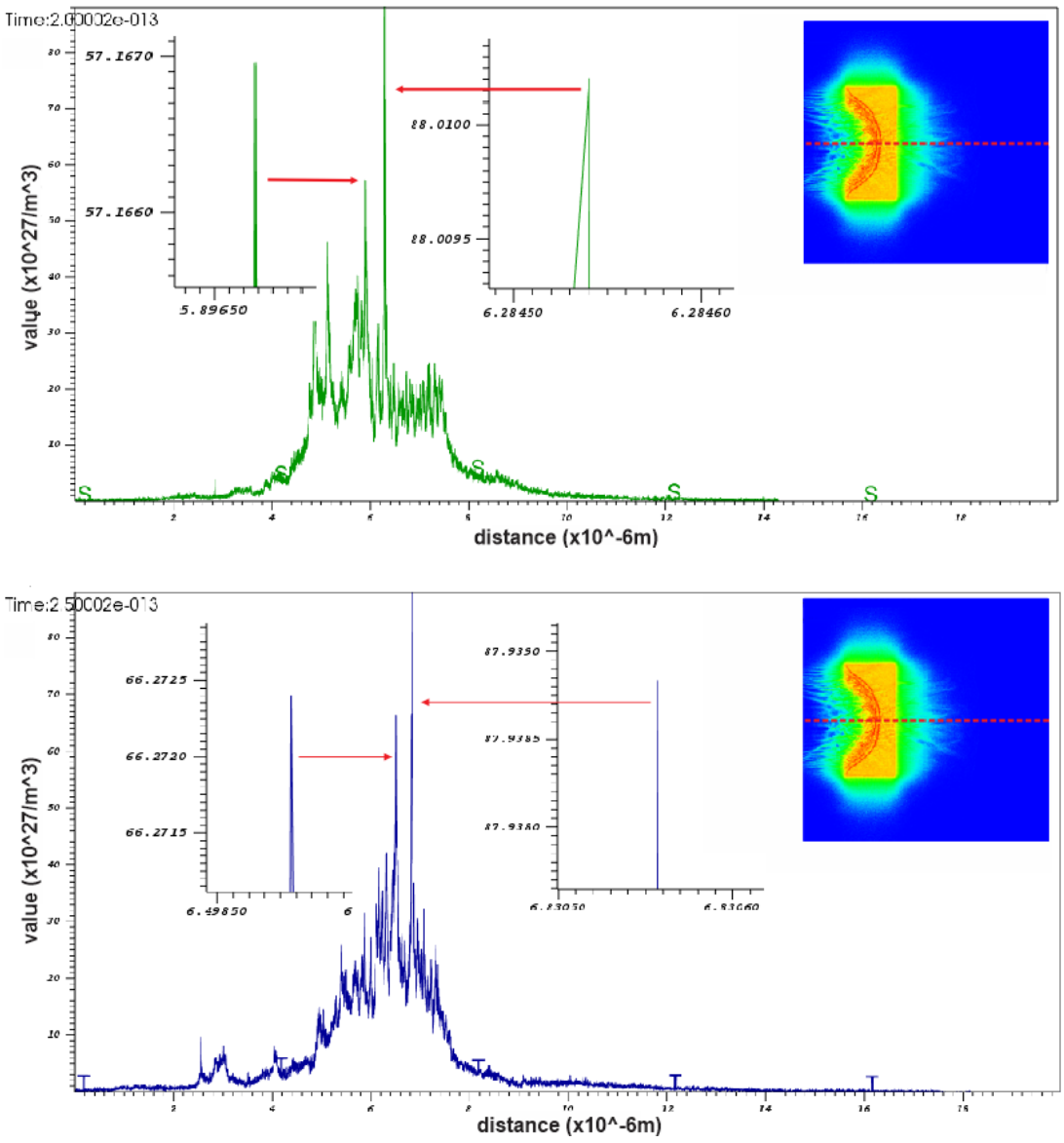

***Figure 5-11*:** lineouts of the electrons density for time 200*fs* (up) and 250*fs* (down). The density spikes show the formed electrostatic collisionless shock as it propagates through the target. On the top right, the pseudocolor of electron density is presented.

Two consecutive lineouts of the density of electrons at 50*fs* are presented in *figure 5-11*, where the position of the shock fronts in 200*fs* and 250*fs* of the simulation, is shown.

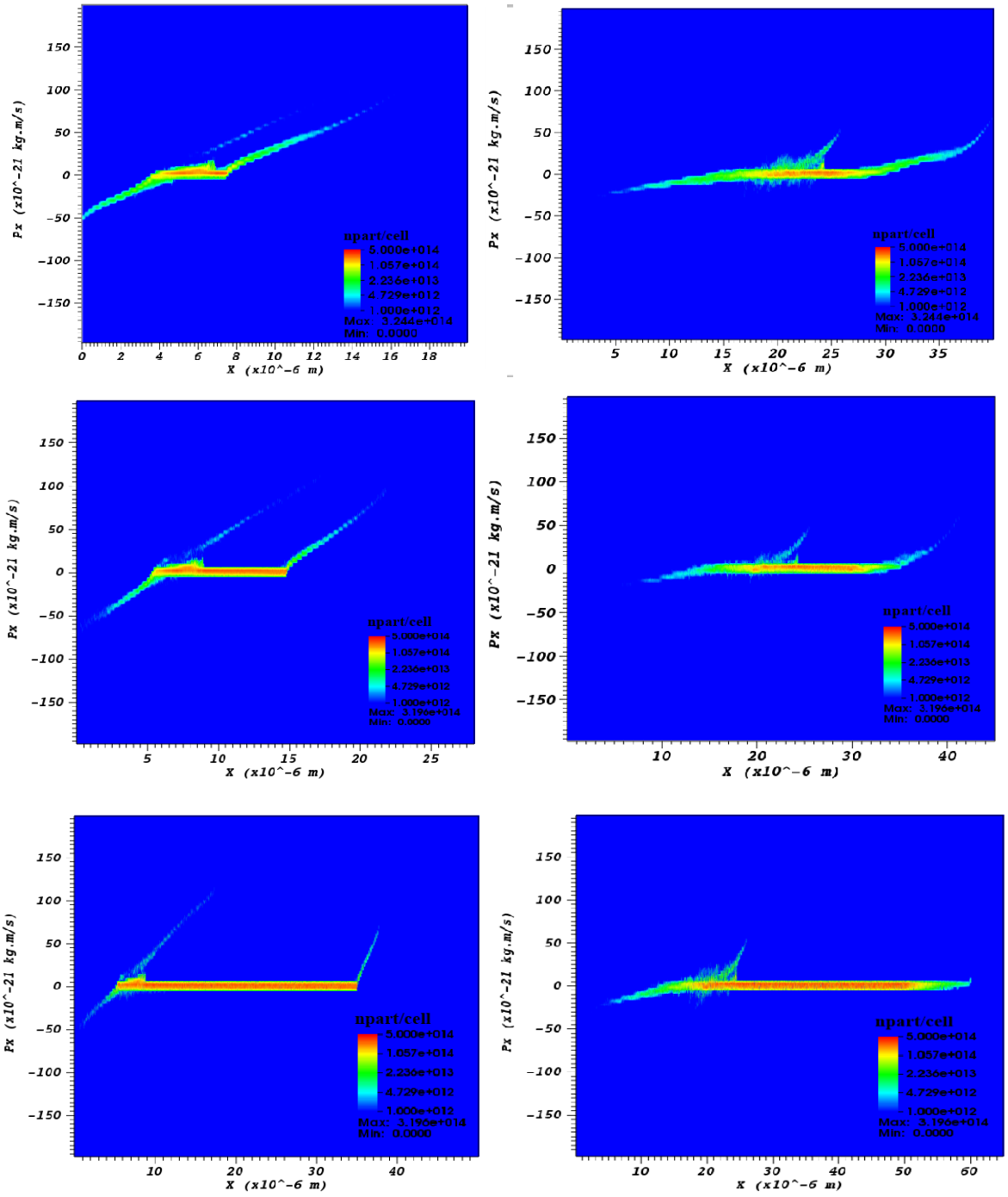

***Figure 5-12*:** proton momentum space at 250*fs* of the simulation. On the Top the 5μm, middle the 10μm and bottom the 30μm targets. The no preplasma scenarios are shown on the left column. Front and rear preplasma scenarios are presented on the right column. The high momentum spikes, show where the ions are accelerated from, while the colorization shows the number of particles/cell.

In *figure 5-12* the x-component of proton momentum as a function of distance, for all targets with and without preplasma expansion, are demonstrated. The coloring corresponds to the number of protons per cell. It appears that for the non-preplasma target scenario (left column) protons at the

rear of the target acquire great momentum $p > 100 * 10^{-21}\ kg * m/s$ which corresponds to moderate relativistic velocity $v_r > 5.86 * 10^7 m/s$.

$$v_r = \sqrt{\frac{p^2 m_e^2}{1 + p^2/m^2 c^2}} \tag{5.3}$$

Protons are accelerated in both front and rear of the target. In the preplasma scenario, presented at the right column, the TNSA is highly suppressed, while protons accelerated by shock in the front of the target, acquire moderate momentum.

The proton kinetic energy spectra for 5μm to 30μm targets for both scenarios, interacting with a pulse of 25*fs* duration, is presented in *figure 5-13*. This was performed by accruing the protons momentum spreadsheet by the *VisIt* [58] post-processing software. The final graphs were plotted by the help of an in-housed algorithm developed in *Matlab* [59]. The momentum spreadsheets were initially linearly scanned. The protons of the same momentum were counted, and the computed relativistic momentum was converted to kinetic energy and plotted to a spectra, as presented in *figure 5-13.* The cut off energy for the no preplasma scenario predicts that the optimum target is the 5μm with a cut off energy up to 37*MeV*. As the target thickness increases the proton cut off energy decreases, approaching the 27*MeV* for the 30μm target.

In the preplasma scenario the proton cut off energies are significantly lower, from 10*MeV* for 10μm thick targets, to above 5*MeV* for 30μm thick targets, which comes close to the experimental results. It has been shown that for low contrast ratio systems, thicker targets are preferable for proton acceleration due to their resilience to the intense nanosecond prepulse. Although there is a certain optimum thickness that above that proton energies will start to diminish again. This thickness is predicted to be about 10μm for *ns* prepulses [45]. This comes in agreement with the simulation results, where for the front and rear prepulse scenario, the maximum cut off energies come from the 10μm thick target. It should be noticed that this model assumes an intact target with preplasma expansion, without taking into account the possibility of a destroyed target, *ps* before the arrival of the main pulse, as it was observed during the experiments.

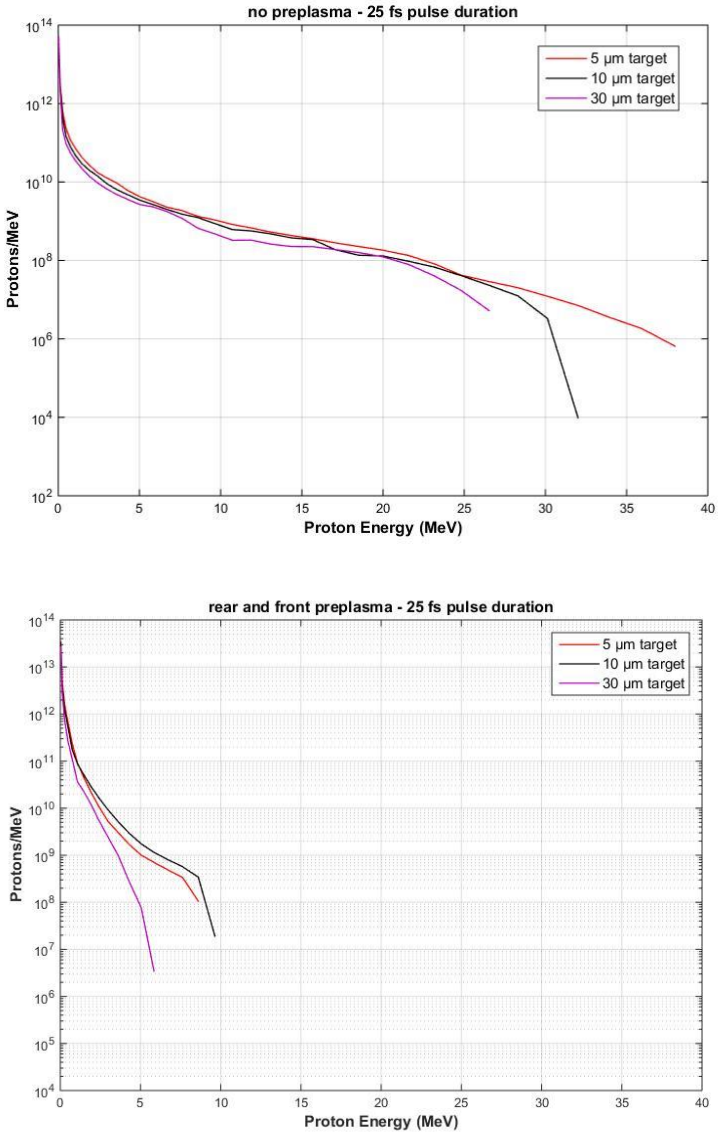

***Figure 5-13*:** Protons/*MeV* as a function of proton cut off energy for 5 to 30μm targets without preplasma (up) and with preplasma expansion (down), of the interaction with a pulse of 25*fs* duration.

The simulation overestimates the number of protons/*MeV*. The main reason of this overestimation is that the target was simulated as explicitly pre-ionized hydrogen, while the protons are accelerated from the thin contamination layers on the front and rear of the target, where the density of hydrogen is way lower. Even though, the cut-off energies were overestimated, possibly due to the assumption of a 3μm focal spot FWHM (the focal spot was accurately measured to be 3μm by the profile camera, though during the experiments retro-focus imaging provided lower accuracy

on the focusing conditions), the model provide us with accurate comparative information of the effects of preplasma expansion in ion acceleration.

The effect of different pulse durations was also investigated. Simulations for all the previously presented scenarios, interacting with a pulse of 80*fs* duration, were performed. These results are demonstrated in *figure 5-14*.

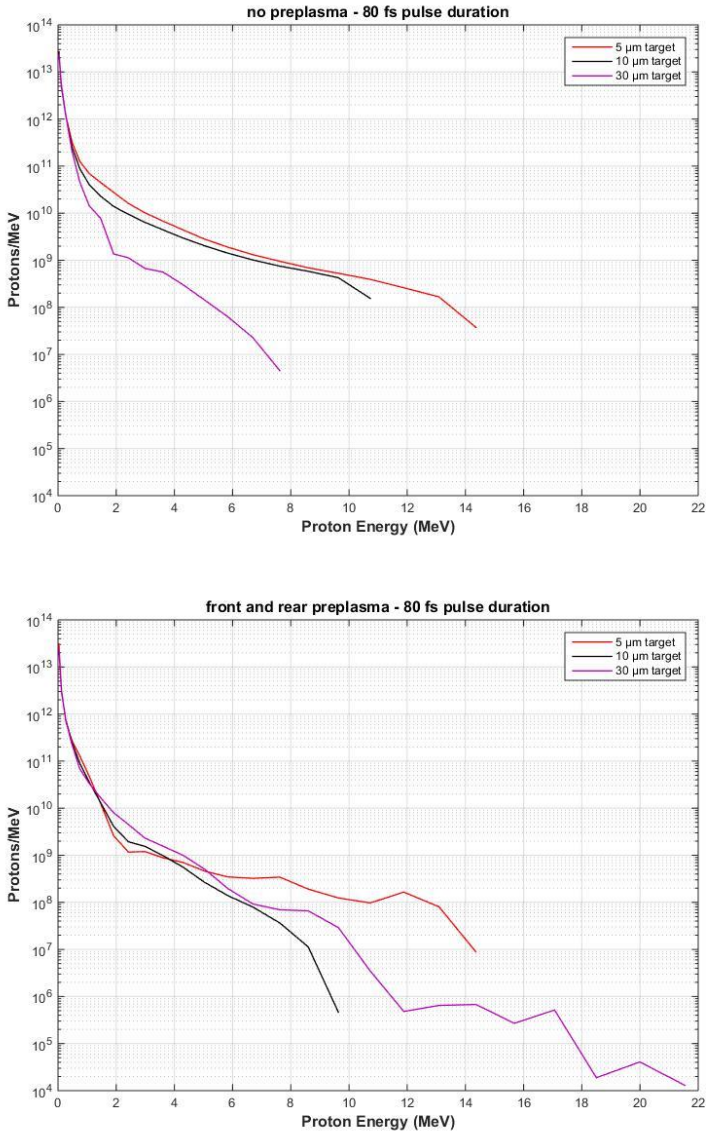

***Figure 5-14*:** Protons/*MeV* as a function of proton cut off energy for 5 to 30μm targets without preplasma (top) and with preplasma expansion (bottom), of the interaction with a pulse of 80*fs* duration.

For the no-preplasma scenario, the maximum cut off energies concern the 5μm thick target. Concluding that for high contrast ratio laser pulses, ion acceleration yields higher energies for

thinner targets independently of the pulse duration. The Protons/*MeV* seem to drop faster for the preplasma expansion, while the proton cut-off energies were unexpectedly high. In order to understand the similarity in cut-off energies of 5 and 10μm thick targets, between preplasma and no preplasma counterparts, their phase spaces must be examined.

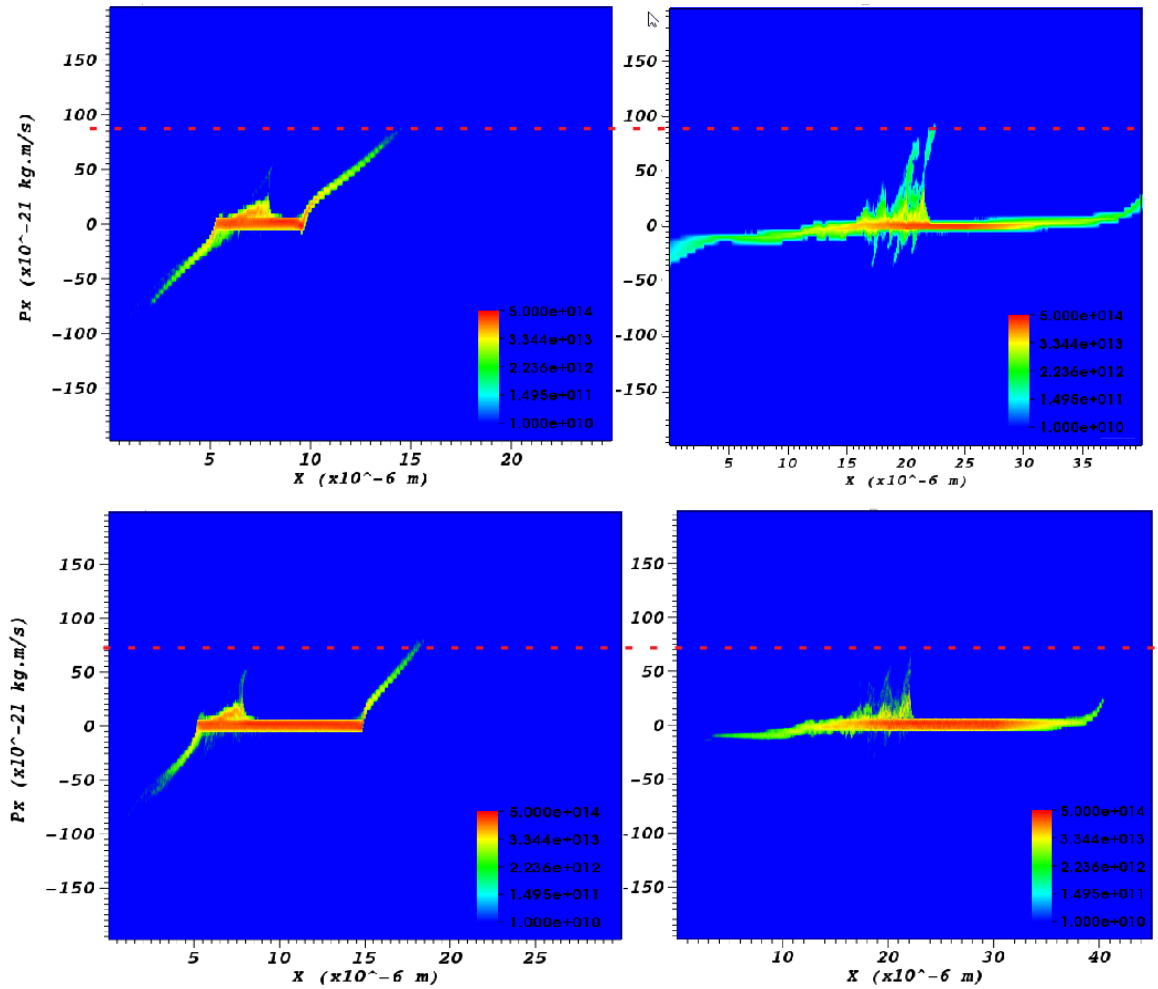

***Figure 5-15*:** Momentums of 10 and 30μm targets. On the top the 10μm target and the 30μm on bottom. Left the no preplasma expansion cases and right the preplasma expansion cases.

As presented in *figure 5-15*, the energies of protons accelerated in the rear of the target by TNSA (left) happens to be very close to those of protons accelerated in the front of the target by shock acceleration. This wasn't observed on the 25*fs* pulses, where the proton energies from each mechanism were usually different. Finally, the protons energy for the 30μm targets appear to be high compared to their 25*fs* counterparts, even though the high energy protons are in the region

below 10^6Protons/*MeV*. A more realistic model of the target, to further approximate the experimental results should be implemented.

The electrons/*MeV* as a function of electron energies are plotted in *figures 5-16* (up) for 5μm - 30μm targets and 25*fs* pulse duration and (down) for 80*fs* pulse duration. The energies from the simulations are close to those predicted by ponderomotive scaling. It is observed that electron cut off energies have low sensitivity to the other parameters of the simulation.

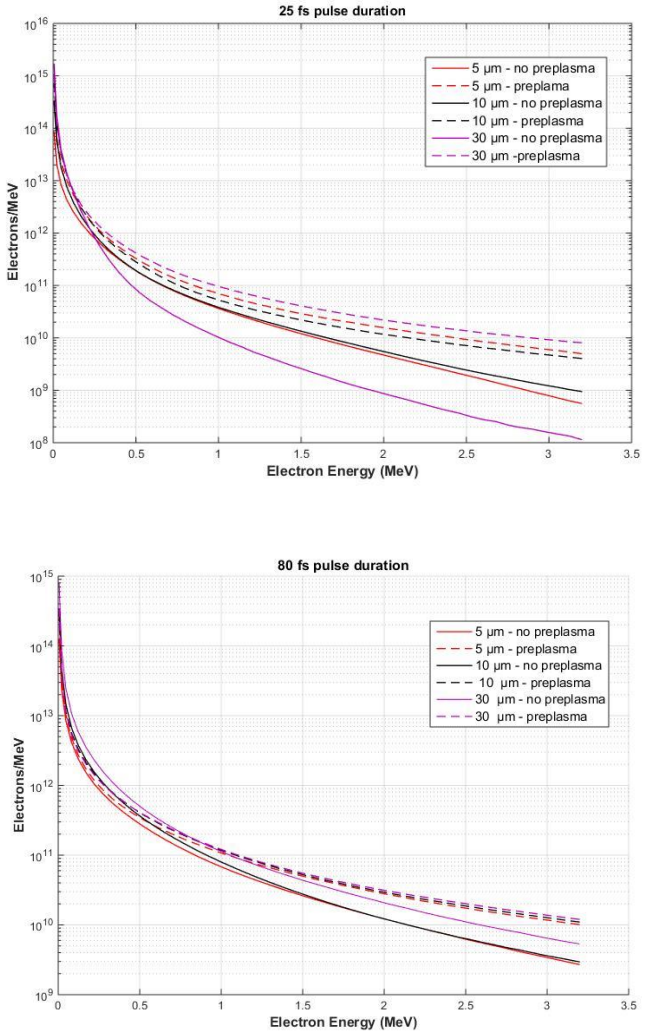

***Figure 5-16*:** Electrons/*MeV* as a function of electron energy for 5 to 30μm targets with front and rear preplasma expansion interacting with (top) 25*fs* pulse and (bottom) a pulse of 80*fs* duration.

5.4 The Aluminum Material Model

In this comparative parametric study, the simplistic 2D pre-ionized hydrogen model, provided us with qualitative information about the effects of preplasma expansion, target thickness and pulse duration, on the acceleration of the protons. In order to properly simulate our experimental results, as well as to further study the interaction of super intense *fs* pulses with solid targets, a more realistic model was implemented.

The target was modeled as partially pre-ionized Aluminum (Al^{+4}) [60] with electron density $n =$ 10 x n_c. The hydrogen was considered trapped in contamination layers [61] of 100*nm* in front and rear of the target. The density of hydrogen was set to be $n_H = n * 10^{-1}$[62]. The focal spot of the laser was loosened to 4μm FWHM, to compensate for the insufficient accuracy of the retro imaging, when focusing the laser into the target. The resulting laser intensity on the focal spot was 3 x $10^{20} W/cm^2$ (a_0=11.8) for 25*fs* pulse and $10^{20} W/cm^2$ (a_0=6.9) for 80*fs* pulse. With this model, two simulations were performed. The scenario of 30μm target with preplasma expansion interacting with the 80*fs* pulse, that yielded the highest proton energies during the experiments, revealed protons accelerated only in the front contamination layer of the target, as shown in *figure 5-17*.

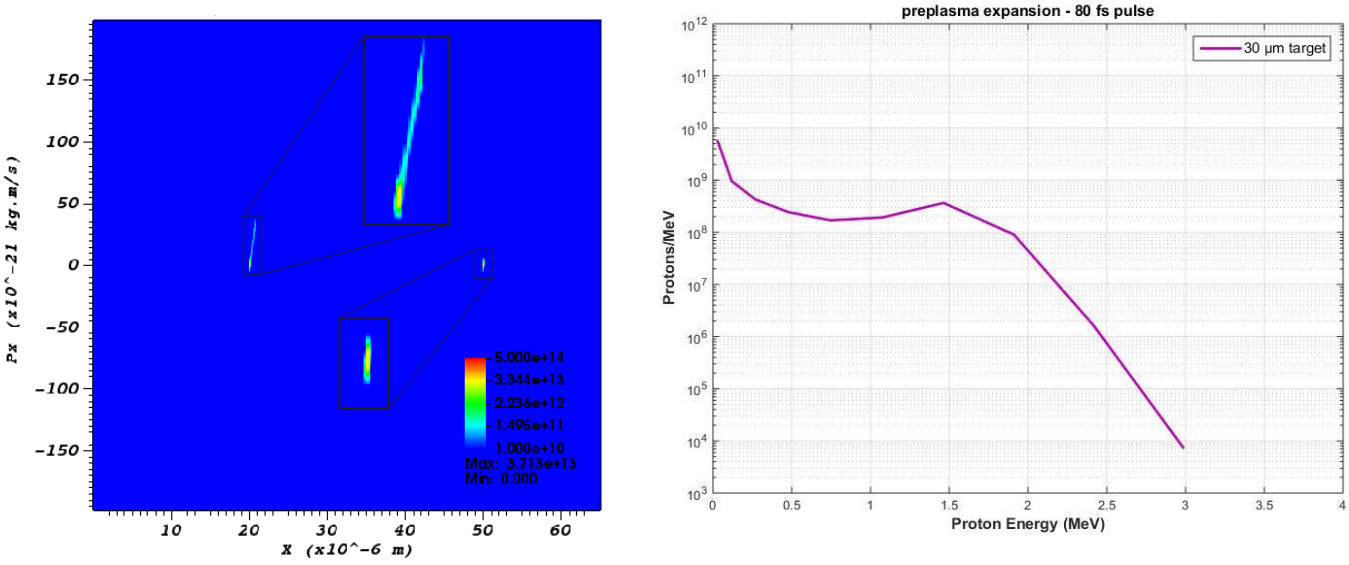

Figure 5-17: The phase space of 30μm target, interacting with 80*fs* pulse (left). Proton/*MeV* as a function of proton cut off energies (right).

The cut-off proton energy was 3*MeV*, which is in good agreement with the corresponding experimental measurements. Protons/*MeV* are in the same order of magnitude measured in CR39 surface.

The next scenario considered the parameters that were determined to be the optimal for ion acceleration from the parametric scan. The target was 5μm thick with no preplasma expansion, interacting with a 25*fs* pulse.

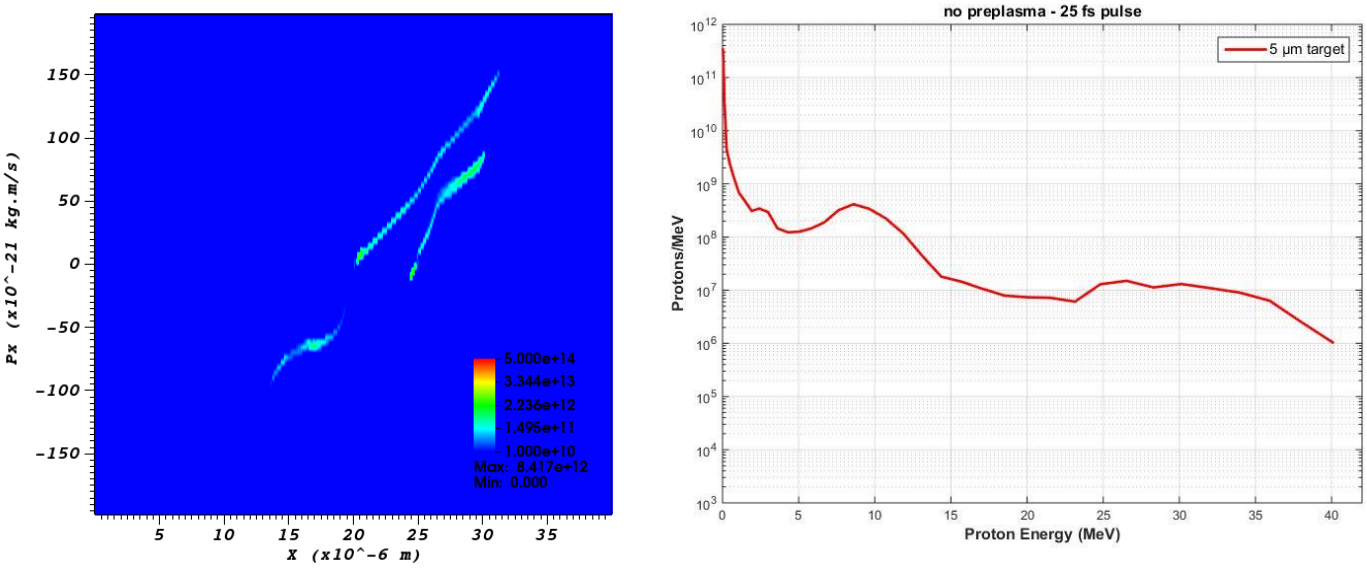

Figure 5-18: The phase space of 5μm target, interacting with 25*fs* pulse (left). Proton/*MeV* as a function of proton cut off energies (right).

For this scenario, the resulting cut off energies were similar to the hydrogen model of 5μm target interacting with 25*fs* pulse (*figure 5-13*). The most energetic ions came from the front of the target, while protons/*MeV* were two orders of magnitude lower. *Figure 5-19* presents the proton density of the 5μm Al target front and rear contamination layers at 250*fs* of the simulation. The front surface accelerated protons surpass the TNSA protons, having acquired greater momentum as already shown in *figure 5-13.*

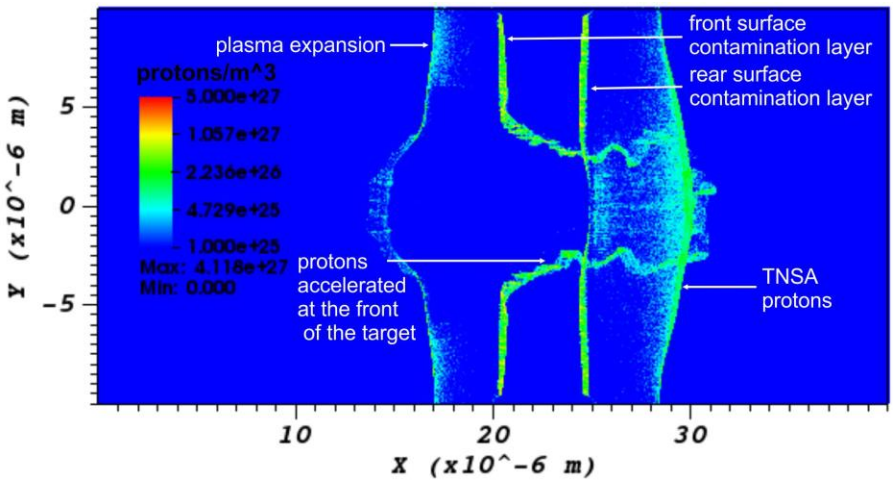

***Figure 5-19**:* Proton density of the 5μm Al target front and rear contamination layers at 250fs of the simulation.

Finally, it should be noted that a preplasma free interaction requires the installation of multiple plasma mirrors. Each plasma mirror reduces the laser energy by about 20%. For the high contrast scenario, the laser energy ending on the targets will be sufficiently lower, resulting to lower proton cut off energies than predicted. This was not considered during these simulations, in order to study the preplasma effects on the proton cut off energies under the same conditions. The effect of different pulse energies, interacting a 5μm target without preplasma expansion, on the proton cut off energy is presented in *figure 5-20*.

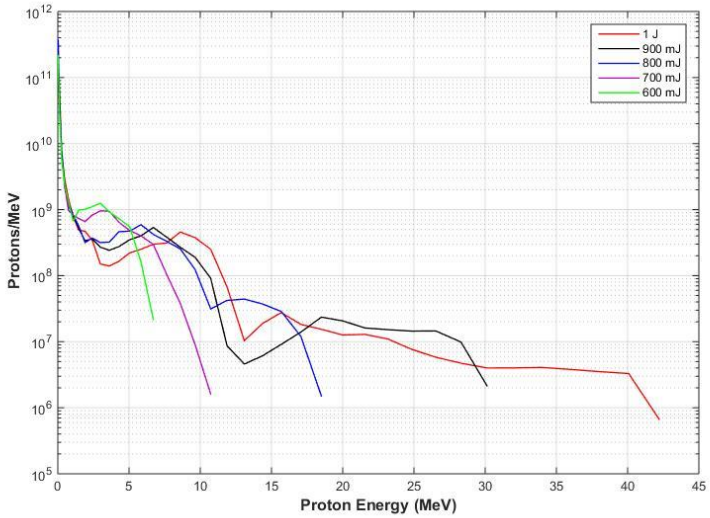

Figure 5-20: Protons/MeV as a function of proton energy for 25fs pulses of 1J to 600mJ energy.

This spectrum was acquired by coarse simulations (20 x 20*nm* cells) where the Debye length was not resolved.

The aluminum model provided more accurate information about the effects of preplasma on proton acceleration while it agrees to the experimental results. The simulations of the rest of the cases should be performed in the future.

Chapter 6

6 Conclusions

In this thesis, the generation of energetic particle beams was investigated. Experiments were performed by the Zeus 45*TW* laser beam in IPPL, irradiating thin aluminum foils with pulses of few *fs* duration at intensities exciding $10^{20} W/cm^2$. A parametric scan was performed were targets of different thicknesses were irradiated by pulses of 25-150*fs* duration, while various diagnostics were used to measure the proton and electron energy spectrum. Protons of 2*MeV* energy and electrons of hundreds of *KeV* were measured.

The effects of laser contrast ratio and early preplasma development in front and rear of the target were studied via PIC simulations. The results revealed the contribution of different acceleration mechanisms based on the initial condition of the targets and made clear the importance of high contrast ratio pulses for efficient TNSA experiments. To achieve this contrast, a double plasma mirror set up may be used. Plasma mirrors allow the low intensity prepulse to pass through them, while reflecting the higher intensities, improve the contrast ratio at about two orders of magnitude per mirror.

A more realistic PIC simulation model, in order to accurately predict the experimental results, should be further developed. 3D PIC simulation of an initially unionized Al target, with a detailed description of the composition of the contamination layer in hydrogen, carbon and other contaminants, will be further developed.

References

[1] T.H. Maiman, *Stimulated Optical Radiation in Ruby*, Nature 187, 493 (1960).

[2] Strickland, D., & Mourou, G. (1985). Compression of amplified chirped optical pulses. *Optics communications*, *55*(6), 447-449.

[3] Conseil Europ´een pour la Recherche Nucl´eaire: www.cern.ch (2007).

[4] Geddes, C. G. R., Toth, C., Van Tilborg, J., Esarey, E., Schroeder, C. B., Bruhwiler, D., ... & Leemans, W. P. (2004). High-quality electron beams from a laser wakefield accelerator using plasma-channel guiding. *Nature*, *431*(7008), 538.

[5] Leemans, W. P., Nagler, B., Gonsalves, A. J., Toth, C., Nakamura, K., Geddes, C. G., ... & Hooker, S. M. (2006). GeV electron beams from a centimetre-scale accelerator. *Nature physics*, *2*(10), 696.

[6] Malka, V., Fritzler, S., Lefebvre, E., d'Humières, E., Ferrand, R., Grillon, G., ... & Hulin, D. (2004). Practicability of protontherapy using compact laser systems. *Medical physics*, *31*(6), 1587-1592.

[7] Murakami, M., Hishikawa, Y., Miyajima, S., Okazaki, Y., Sutherland, K. L., Abe, M., ... & Yamagiwa, M. (2008, June). Radiotherapy using a laser proton accelerator. In *AIP conference proceedings* (Vol. 1024, No. 1, pp. 275-300). AIP.

[8] Linz, U., & Alonso, J. (2007). What will it take for laser driven proton accelerators to be applied to tumor therapy?. *Physical Review Special Topics-Accelerators and Beams*, *10*(9), 094801

[9] Wagner, F., Deppert, O., Brabetz, C., Fiala, P., Kleinschmidt, A., Poth, P., ... & Stöhlker, T. (2016). Maximum proton energy above 85 mev from the relativistic interaction of laser pulses with micrometer thick ch 2 targets. *Physical review letters*, *116*(20), 205002.

[10] Kim, I. J., Pae, K. H., Choi, I. W., Lee, C. L., Kim, H. T., Singhal, H., ... & Jeong, T. M. (2016). Radiation pressure acceleration of protons to 93 MeV with circularly polarized petawatt laser pulses. *Physics of Plasmas*, *23*(7), 070701.

[11] Li, C. K., Séguin, F. H., Frenje, J. A., Rygg, J. R., Petrasso, R. D., Town, R. P. J., ... & Patel, P. K. (2006). Measuring E and B fields in laser-produced plasmas with monoenergetic proton radiography. *Physical review letters*, *97*(13), 135003.

[12] Romagnani, L., Fuchs, J., Borghesi, M., Antici, P., Audebert, P., Ceccherini, F., ... & Mora, P. (2005). Dynamics of electric fields driving the laser acceleration of multi-MeV protons. *Physical review letters*, *95*(19), 195001

[13] Tabak, M., Hammer, J., Glinsky, M. E., Kruer, W. L., Wilks, S. C., Woodworth, J., ... & Mason, R. J. (1994). Ignition and high gain with ultrapowerful lasers. *Physics of Plasmas*, *1*(5), 1626-1634.

[14] National Ignition Facility Programs: www.llnl.gov/nif (2007).

[15] HiPER, High Power laser Energy Reaseach facility: www.hiperlaser.eu (2007).

[16] Clark, E. L. (2002). Measurements of energetic particles from ultraintense laser plasma interactions.

[17] Silva, L. O., Marti, M., Davies, J. R., Fonseca, R. A., Ren, C., Tsung, F. S., & Mori, W. B. (2004). Proton shock acceleration in laser-plasma interactions. *Physical Review Letters, 92*(1), 015002.

[18] Robinson, A. P. L., Zepf, M., Kar, S., Evans, R. G., & Bellei, C. (2008). Radiation pressure acceleration of thin foils with circularly polarized laser pulses. *New journal of Physics, 10*(1), 013021.

[19] Ashkin, A. (1970). Acceleration and trapping of particles by radiation pressure. *Physical review letters*, *24*(4), 156.

[20] Qiao, B., Zepf, M., Borghesi, M., Dromey, B., Geissler, M., Karmakar, A., & Gibbon, P. (2010). Radiation-pressure acceleration of ion beams from nanofoil targets: The leaky light-sail regime. *Physical review letters*, *105*(15), 155002

[21] Zepf, M., Borghesi, M., McKenna, P., Neely, D., Najmudin, Z., Robinson, A. P. L., ... & Doria, D. (2010). Radiation Pressure Acceleration in the Light-Sail Regime. In *37th EPS Conference on Plasma Physics, Dublin, Ireland*.

[22] Agostini, P., Fabre, F., Mainfray, G., Petite, G., & Rahman, N. K. (1979). Free-free transitions following six-photon ionization of xenon atoms. Physical Review Letters, 42(17), 1127.

[23] Paul G. Short Pulse Laser Interaction with Matter

[24] Keldysh, L. V. (1965). Ionization in the field of a strong electromagnetic wave. *Sov. Phys. JETP*, *20*(5), 1307-1314.

[25] Wilks, S. C., & Kruer, W. L. (1997). Absorption of ultrashort, ultra-intense laser light by solids and overdense plasmas. *IEEE Journal of Quantum Electronics*, *33*(11), 1954-1968.v

[26] Kruer, W. L. (1988). 'The physics of Laser Plasma Interaction'Addison-Wesley Publ.

[27] Brunel, F. (1987). Not-so-resonant, resonant absorption. *Physical Review Letters*, *59*(1), 52.

[28] Kato, S., Bhattacharyya, B., Nishiguchi, A., & Mima, K. (1993). Wave breaking and absorption efficiency for short pulse p-polarized laser light in a very steep density gradient. *Physics of Fluids B: Plasma Physics, 5*(2), 564-570.

[29] Kruer, W., & Estabrook, K. (1985). J× B heating by very intense laser light. *The Physics of fluids*, *28*(1), 430-432.

[30] Malka, G., & Miquel, J. L. (1996). Experimental confirmation of ponderomotive-force electrons produced by an ultrarelativistic laser pulse on a solid target. *Physical Review Letters*, *77*(1), 75

[31] Roth, M., and M. Schollmeier. "Ion acceleration-target normal sheath acceleration." *arXiv preprint arXiv:1705.10569* (2017).

[32] Wilks, S. C., Langdon, A. B., Cowan, T. E., Roth, M., Singh, M., Hatchett, S., ... & Snavely, R. A. (2001). Energetic proton generation in ultra-intense laser–solid interactions. *Physics of plasmas*, *8*(2), 542-549.

[33] Clark, E. L., Krushelnick, K., Davies, J. R., Zepf, M., Tatarakis, M., Beg, F. N., ... & Dangor, A. E. (2000). Measurements of energetic proton transport through magnetized plasma from intense laser interactions with solids. *Physical Review Letters*, *84*(4), 670.

[34] Snavely, R. A., Key, M. H., Hatchett, S. P., Cowan, T. E., Roth, M., Phillips, T. W., ... & Wilks, S. C. (2000). Intense high-energy proton beams from petawatt-laser irradiation of solids. *Physical Review Letters*, *85*(14), 2945.

[35] Maksimchuk, A., Gu, S., Flippo, K., Umstadter, D., & Bychenkov, V. Y. (2000). Forward ion acceleration in thin films driven by a high-intensity laser. *Physical Review Letters*, *84*(18), 4108.

[36] Hegelich, B. M., Albright, B. J., Cobble, J., Flippo, K., Letzring, S., Paffett, M., ... & Fernández, J. C. (2006). Laser acceleration of quasi-monoenergetic MeV ion beams. *Nature*, *439*(7075), 441.

[37] Schwoerer, H., Pfotenhauer, S., Jäckel, O., Amthor, K. U., Liesfeld, B., Ziegler, W., ... & Esirkepov, T. (2006). Laser-plasma acceleration of quasi-monoenergetic protons from microstructured targets. *Nature*, *439*(7075), 445.

[38] G. Hoffmeister. Influencing laser-accelerated ions by femtosecond-laser desorption, Doctoral Thesis, TU Darmstadt (2014).

[39] Hegelich, M., Karsch, S., Pretzler, G., Habs, D., Witte, K., Guenther, W., ... & Geissel, M. (2002). MeV ion jets from short-pulse-laser interaction with thin foils. *Physical review letters*, *89*(8), 085002.

[40] Passoni, M., & Lontano, M. (2008). Theory of light-ion acceleration driven by a strong charge separation. *Physical review letters*, *101*(11), 115001

[41] Mora, P. (2003). Plasma expansion into a vacuum. *Physical Review Letters*, *90*(18), 185002.

[42] J. F. Ziegler, http://www.srim.org/ (2006).

[43] Groom, D. E., & Klein, S. R. (2000). Passage of particles through matter. *The European Physical Journal C-Particles and Fields*, *15*(1-4), 163-173.

[44] Batani, D., Jafer, R., Redaelli, R., Dezulian, R., Lundh, O., Lindau, F., ... & McKenna, P. (2010). Effects of laser prepulse on proton generation. *Nuclear Instruments and Methods in Physics Research Section A: Accelerators, Spectrometers, Detectors and Associated Equipment*, *620*(1), 76-82.

[45] Kaluza, M., Schreiber, J., Santala, M. I., Tsakiris, G. D., Eidmann, K., Meyer-ter-Vehn, J., & Witte, K. J. (2004). Influence of the laser prepulse on proton acceleration in thin-foil experiments. *Physical review letters*, *93*(4), 045003.

[46] Cartwright, B. G., Shirk, E. K., & Price, P. B. (1978). A nuclear-track-recording polymer of unique sensitivity and resolution. *Nuclear Instruments and Methods*, *153*(2-3), 457-460.

[47] McLaughlin, W. L., Yun-Dong, C., Soares, C. G., Miller, A., Van Dyk, G., & Lewis, D. F. (1991). Sensitometry of the response of a new radiochromic film dosimeter to gamma radiation and electron beams. *Nuclear Instruments and Methods in Physics Research Section A: Accelerators, Spectrometers, Detectors and Associated Equipment*, *302*(1), 165-176.

[48] Bolton, P. R., Borghesi, M., Brenner, C., Carroll, D. C., De Martinis, C., Fiorini, F., ... & Giove, D. (2014). Instrumentation for diagnostics and control of laser-accelerated proton (ion) beams. *Physica Medica*, *30*(3), 255-270.

[49] M. Tatarakis, Ph.D. theses, Imperial College of London (1996).

[50] www.elimpex.com/new/products/radiation_therapy/Gafchromic/ Last visited (2019, June 19)

[51] https://rt-safe.com/ Last visited (2019, June 19)

[52] Nektarios A. Papadogiannis Ph.D thesis (1996). Interaction of Ultrashort Intense Laser Pulses with Metallic Surfaces

[53] T. D. Arber, K. Bennett, C. S. Brady, A. Lawrence-Douglas, M. G. Ramsay, N. J. Sircombe, P. Gillies, R. G. Evans, H. Schmitz, A. R. Bell and C. P. Ridgers, "A particle-in-cell code for laser-plasma interactions: test problems, convergence and accuracy," Journal of Computational Physics, 2014.

[54] Pukhov, A. (2001). Three-dimensional simulations of ion acceleration from a foil irradiated by a short-pulse laser. *Physical review letters*, *86*(16), 3562.

[55] Turrell, A. E., Sherlock, M., & Rose, S. J. (2015). Ultrafast collisional ion heating by electrostatic shocks. *Nature communications*, *6*, 8905.

[56] Forslund, D. W., & Shonk, C. R. (1970). Formation and structure of electrostatic collisionless shocks. *Physical Review Letters*, *25*(25), 1699.

[57] Stefano A. (2003) Inertial fusion

[58] https://wci.llnl.gov/simulation/computer-codes/visit/ Last visited (2019, June 19)

[59] https://www.mathworks.com/ Last visited (2019, June 19)

[60] Kumar, A., & Mathew, V. (2018, May). Computational study of proton acceleration from the laser irradiated metal substrate. In *AIP Conference Proceedings* (Vol. 1953, No. 1, p. 140011). AIP Publishing.

[61] Ferri, J., Siminos, E., & Fülöp, T. (2019). Enhanced target normal sheath acceleration using colliding laser pulses. *Communications Physics*, *2*(1), 40.

[62] Sinigardi, S., Babaei, J., & Turchetti, G. (2018). TNSA proton maximum energy laws for 2D and 3D PIC simulations. *Nuclear Instruments and Methods in Physics Research Section A: Accelerators, Spectrometers, Detectors and Associated Equipment*.